

Joint Spatial-Angular Sparse Coding for dMRI with Separable Dictionaries

Evan Schwab, René Vidal, and Nicolas Charon

Center for Imaging Science, Johns Hopkins University, Baltimore, MD USA

Abstract

Diffusion MRI (dMRI) provides the ability to reconstruct neuronal fibers in the brain, *in vivo*, by measuring water diffusion along angular gradient directions in q -space. High angular resolution diffusion imaging (HARDI) can produce better estimates of fiber orientation than the popularly used diffusion tensor imaging, but the high number of samples needed to estimate diffusivity requires lengthy patient scan times. To accelerate dMRI, compressed sensing (CS) has been utilized by exploiting a sparse dictionary representation of the data, discovered through sparse coding. The sparser the representation, the fewer samples are needed to reconstruct a high resolution signal with limited information loss, and so an important area of research has focused on finding the sparsest possible representation of dMRI. Current reconstruction methods however, rely on an angular representation *per voxel* with added spatial regularization, and so, the global level of sparsity can be no less than the number of voxels. Therefore, state-of-the-art dMRI CS frameworks may have a fundamental limit to the rate acceleration that can be achieved. In contrast, we propose a joint spatial-angular representation of dMRI that will allow us to achieve levels of global sparsity that are below the number of voxels. A major challenge, however, is the computational complexity of solving a global sparse coding problem over large-scale dMRI. In this work, we present novel adaptations of popular sparse coding algorithms that become better suited for solving large-scale problems by exploiting spatial-angular separability. Our experiments show that our method achieves significantly sparser representations of HARDI than the state-of-the-art which has the potential to increase HARDI acceleration to new levels.

Keywords: sparse coding; separable dictionaries; Kronecker product; diffusion MRI

1. Introduction

Diffusion magnetic resonance imaging (dMRI) is a medical imaging modality used to analyze neuroanatomical biomarkers for brain diseases such as Alzheimer's. dMRI are 6D signals consisting of a set of 3D spatial MRI volumes acquired in k -space that are each weighted with a different diffusion signal measured in q -space.

- 5 In each voxel of a brain dMRI, the q -space diffusion signals are reconstructed to estimate orientations and integrity of neuronal fiber tracts, *in vivo*. Different dMRI protocols measure q -space in different ways. For example, diffusion spectrum imaging (DSI) [62] measures q -space densely on a 3D grid. Alternatively, diffusion tensor imaging (DTI) [5] simplifies acquisition by restricting q -space measurements to the unit sphere. High angular resolution diffusion imaging (HARDI) [61] also restricts measurements to the unit sphere, but increases

10 the angular resolution from that of DTI. Multi-Shell HARDI (MS-HARDI) [64] expands its radial range to include multiple spheres, or shells. Since DTI collects the fewest number of measurements, it has become the most widely used clinical dMRI protocol. However, its simple tensor model is unable to capture the complex diffusion profiles in each voxel. On the other hand, protocols like HARDI, MS-HARDI, and especially DSI, collect a higher number of q -space measurements to estimate more accurate diffusion profiles, but suffer from
15 lengthy scan times which makes them not currently suitable for clinical studies.

An ongoing research goal has been to find ways to reduce acquisition times of HARDI, MS-HARDI, or DSI, while maintaining accurate estimations of diffusion. One avenue is from a hardware perspective: maintain dense signal measurement configurations while devising faster physical acquisition techniques like simultaneous multi-slice acquisition [55] and simultaneous image refocusing [51]. The other is from a signal processing
20 perspective: maintain accurate signal reconstructions while devising methods to exploit redundancies in the data and reduce the number of required measurements to accelerate acquisition. This paradigm is known as Compressed Sensing (CS) [18]. Eventually, the two areas may be optimally integrated [56], but our focus will be on advancing the latter by proposing a new approach for finding sparse representations of dMRI signals.

CS is a class of mathematical results and algorithms that exploits sparse representations of signals,
25 discovered through sparse coding, to obtain extremely accurate reconstructions at sub-Nyquist rates. A classical application of CS has been to accelerate structural MRI by subsampling the spatial frequency domain, k -space [30], known as k -space CS or k -CS. These ideas have also been previously applied to dMRI by subsampling the angular frequency domain, q -space, [43] (analogously called q -CS) and more recently, to subsample both k - and q -space [13, 57], commonly called (k, q) -space CS or (k, q) -CS, to further increase
30 acceleration. However, because the goal of dMRI reconstruction is to estimate diffusivity profiles at each voxel, dMRI signals are traditionally represented as a set of voxel-wise q -space signals in the angular domain. Spatial regularization is an important technique used to improve these estimations over an entire dMRI volume [22], and particularly important for (k, q) -CS, but the underlying data representation of dMRI is still angular in prior work. Therefore, when applying sparse coding for dMRI, the sparsest possible global representation over
35 an entire volume can be no less than the number of voxels since at least one dictionary atom would be required to model q -space signals in each voxel. Then, since the minimum number of compressed measurements needed for accurate reconstruction depends on the level of sparsity, state-of-the-art dMRI CS methods may eventually have a fundamental limit to the accelerations that can be achieved by using purely angular representations.

Instead, we propose a joint spatial-angular representation of dMRI that allows global sparsity levels to
40 fall below one atom per voxel by exploiting redundancies in the spatial and angular domains, *jointly*. This can then open up the possibility to overcome the sparsity limits of the state of the art to achieve much higher acceleration rates for dMRI. A major challenge, however, is the computational complexity of solving a massive global sparse coding problem over large-scale dMRI data. Yet, by imposing that our global dictionary be separable over the spatial and angular domains we can greatly improve computational efficiency while
45 preserving good sparsity levels for typical signals. Our main contribution in this paper is a set of novel

adaptations of popular sparse coding algorithms to solve general large-scale sparse coding problems using separable dictionaries. Our experiments on phantom and real HARDI brain data show that it is possible to achieve accurate global HARDI reconstructions with a sparse representation of less than one dictionary atom per voxel, exceeding the theoretical limit of the state of the art in sparse coding. Incorporating this *joint* spatial-angular sparse coding framework into a *joint* (k, q) -CS framework will be the subject of future work.

The remainder of this paper is organized as follows: In Section 2, we review state-of-the-art sparse coding and CS dMRI methods and illustrate the limitations of their performance on a phantom HARDI dataset. In Section 3, we present our joint spatial-angular dMRI representation and formalize the global spatial-angular sparse coding problem. Then, in Section 4, we develop and compare a set of novel sparse coding algorithms using separable dictionaries to efficiently solve our large-scale global optimization. Finally, in Section 5 we provide experimental results showing the performance of our method over the state-of-the-art and conclude with a discussion in Section 6.

2. State of the Art

2.1. Angular (Voxel-Wise) Reconstruction

A dMRI is a 6D signal $\mathcal{S}(v, q)$, where $v \in \Omega \subset \mathbb{R}^3$ is the location of a voxel in the 3D spatial domain Ω and $\vec{q} \in \mathbb{R}^3$ is a point in the so-called q -space.¹ A dMRI signal is measured at a discrete number of voxels, V , and a discrete number of q -space points, G . To better visualize \mathcal{S} , one can view the signal as a set of G diffusion weighted images (DWIs), where for each diffusion weighted q -space point, we acquire a volume $s_{\vec{q}} = s_{\vec{q}}(v)_{v=1}^V = \mathcal{S}(v, \vec{q})_{v=1}^V$. An alternative view is that for each voxel $v \in \Omega$, a vector of G diffusion measurements $s_v = s_v(\vec{q}_g)_{g=1}^G = \mathcal{S}(v, \vec{q}_g)_{g=1}^G$ are acquired at points \vec{q}_g in 3D q -space. The latter interpretation is most common for modeling because a major goal of dMRI reconstruction is to estimate 3D probability distribution functions (PDFs) of fiber tract orientation at each voxel. Accordingly, the signal vector s_v is represented by a q -space basis, $\Gamma = [\Gamma_i(\vec{q})]_{i=1}^{N_\Gamma}$, with N_Γ atoms, such that

$$s_v(\vec{q}) = \sum_{i=1}^{N_\Gamma} \Gamma_i(\vec{q}) a_{i,v}. \quad (1)$$

The dMRI literature has produced a wide array of dMRI reconstruction algorithms for different acquisition protocols, an artillery of q -space bases and varying models for estimating fiber tract PDFs. The vast majority of research reconstructs q -space signals in each voxel with a q -space basis while adding a set of constraints $\mathcal{C}(a_v)$ on the coefficients to enforce desirable properties such as non-negativity of PDFs [53, 63] or angular smoothing [65], solving:

$$a_v^* = \arg \min_{a_v} \frac{1}{2} \|\Gamma a_v - s_v\|_2^2 \quad \text{s.t. } \mathcal{C}(a_v). \quad (2)$$

¹The q -space is the frequency domain associated with the angular domain, while the k -space is the frequency domain associated with the spatial domain.

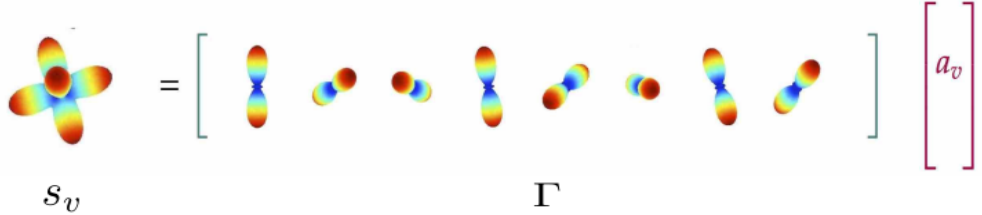


Figure 1: Illustration of voxel-wise angular HARDI representation a_v using a sparsifying dictionary Γ .

60 The constraint of particular interest in our paper is that of enforcing sparsity on the coefficients of the reconstruction, known as *Sparse Coding*, which has applications in CS as well as super-resolution [69] and de-noising [46].

2.2. Angular (Voxel-Wise) Sparse Coding

Sparse coding is a reconstruction problem which seeks a sparse representation, i.e. a coefficient vector with few nonzero elements. Given a sparsifying q -space basis Γ for which the dMRI signal in each voxel is expected to have a sparse representation, the angular (voxel-wise) sparse coding problem can be formulated as:

$$a_v^* = \arg \min_{a_v} \frac{1}{2} \|\Gamma a_v - s_v\|_2^2 \quad \text{s.t.} \quad \|a_v\|_0 \leq K_v, \quad (3)$$

where $\|a_v\|_0$ counts the number of nonzero elements of vector a_v , and K_v is the sparsity level at voxel v . This problem is known to be NP-hard, and therefore the two main methodologies to tackle (3) are *a*) approximate a solution using greedy algorithms such as Orthogonal Matching Pursuit (OMP) [60] or *b*) replace the 0-norm by its convex relaxation l_1 norm and solve either the Basis Pursuit or LASSO problem given by:

$$a_v^* = \arg \min_{a_v} \frac{1}{2} \|\Gamma a_v - s_v\|_2^2 + \lambda \|a_v\|_1 \quad (4)$$

65 using algorithms such as Alternating Direction Method of Multipliers (ADMM) [8] or Fast Iterative Thresholding Algorithm (FISTA) [6], where λ is the trade-off parameter between data fidelity and sparsity. Angular sparse coding and q -CS have been widely researched for dMRI to reduce long acquisition times. Many groups have done extensive work choosing sparsifying q -space bases [36, 43, 2], developing dictionary learning methods [7, 14, 16, 24, 25, 34, 35, 58], and testing q -space subsampling schemes for DSI [25, 38, 33, 37, 47], MS-HARDI [15, 50, 35, 21, 17], HARDI [40, 41, 59, 20, 1] and DTI [29] with promising results in sparsity and measurement reduction for clinical tractography [28, 27]. However, a major limitation for this family of methods is that the sparsest possible representation of an entire dMRI dataset can be no less than the number of voxels since $\|a_v\|_0 \geq 1 \forall v \in \Omega$. In CS applications, this induces fundamental limitations in the amount of subsampling factors that may be achievable in q -space. In practice, the global sparsity level will be much greater than the number of voxels, to account for noise. For example the work of [39, 41] report an average sparsity level of 6 to 10 atoms per voxel. The methods presented in the next section attempt to improve upon these results by exploiting spatial redundancies and reducing measurements in k -space.

2.3. Angular Sparse Coding with Spatial Regularization

Incorporating spatial information into voxel-wise reconstruction is a well utilized technique for increasing the accuracy of reconstruction. The following is a general formulation for including spatial regularization into the angular sparse coding problem:

$$A^* = \arg \min_A \|\Gamma A - S\|_F^2 + \lambda \|A\|_1 + \mathcal{R}(A), \quad (5)$$

where $S = [s_1 \dots s_V] \in \mathbb{R}^{G \times V}$ is the concatenation of signals $s_v \in \mathbb{R}^G$ sampled at G gradient directions over V voxels, $A = [a_1 \dots a_V] \in \mathbb{R}^{N_\Gamma \times V}$ is the concatenation of angular coefficients and $\mathcal{R}(A)$ is a spatial regularizer that depends on the angular representation A . In particular when $\mathcal{R} = 0$, this reduces to solving (4) for all voxels simultaneously. When $\lambda = 0$, this is the general non-sparse reconstruction with spatial coherence (see [22] for example). Some have found incorporating both the angular sparsity constraint $\lambda \|A\|_1$ and spatial coherence $\mathcal{R}(A)$ beneficial for applications such as de-noising [67, 46, 45, 65] and tractography [66].

Spatial regularization within sparse coding is more prominently used for the application of reducing redundancies for CS. For example, [42, 49, 3] enforce spatial smoothing for q -CS while [44, 68] combine q -CS with super-resolution reconstruction of the spatial domain. To further accelerate dMRI, the recent work of [12] combines CS with parallel imaging but reconstructs the signals in k -space and q -space separately in sequence. A joint (k, q) -space reconstruction is important for maintaining coherence throughout the dataset. As such, the works of [4, 56, 13, 57, 32, 31] combine k - and q -CS by adding a data fidelity term for k -space subsampling and an additional spatial sparsity term. In total, however, while each of these works may be applied to different diffusion models and acquisition protocols testing various subsampling schemes, sparsifying transforms and dictionaries, each are based on an angular representation of dMRI data, A , and stem from the same optimization problem formulation (5) with

$$\mathcal{R}(A) = \xi \|\Psi(\Gamma A)\|_1 \quad (6)$$

where $\xi \geq 0$ is an additional trade-off weighting parameter, and $\Psi(\cdot)$ is a sparsifying transform (or dictionary) applied to the spatial domain such as wavelets or the finite difference gradient operator, leading to the usual total variation (TV) norm. In (6), ΓA is a reconstruction of the signal S based on the angular representation A . While adding these spatial and angular sparsity terms may exploit redundancies in both the spatial and angular domains, because they are separate disjoint terms the minimal global sparsity level will be still limited by the size of the data since $\|A\|_0$ should be greater than V and $\|\Psi(\Gamma A)\|_0$ should be greater than G . Indeed, when $\|A\|_0 < V$, there must exist voxels v such that $a_v = 0$, leading to a zero valued signal s_v (column of S) in that voxel. Likewise, when $\|\Psi(\Gamma A)\|_0 < G$, there must exist some gradient directions, \vec{q}_g , such that the signal in the entire volume $s_{\vec{q}}$ (rows of S) equals zero. This becomes a problem because zero valued signals are not physically representative of real dMRI data. This also becomes a heuristic limitation of prior methods for appropriately choosing trade-off parameters λ and ξ that result in a physically accurate sparsity level. In the next section we will explicitly show this sparsity limitation on phantom data.

		Sparse Coding			
		Spatial	Angular	Spatial + Angular	Joint Spatial-Angular
CS	k	[30]			
	q		[47, 3, 43, 16, 17, 2, 1, 66, 44, 68]		
	(k, q)			[4, 56, 13, 57, 32, 31]	Proposed

Table 1: Summary of the many state-of-the-art dMRI sparse reconstruction methods organized by domains of sparse coding and CS subsampling. The literature has provided a natural extension from k -CS in MRI using spatial sparse coding to q -CS in dMRI angular sparse coding. However, for (k, q) -CS, the state of the art enforce sparsity in the spatial and angular domains separately, (called “Spatial + Angular” Sparse Coding) with a purely angular representation. In contrast, the proposed work considers a joint spatial-angular representation for sparse coding which is a more natural model for joint (k, q) -CS.

Table 1 organizes the recent literature’s usages of sparse coding and CS for dMRI and places the proposed work in context compared to the state of the art. There we use the term “Spatial + Angular” Sparse Coding to emphasize that the state of the art perform both spatial and angular sparse coding, but not jointly. In light of a joint (k, q) -CS, a disjoint set of spatial and angular sparsifying transforms may also not be the most natural choice from a classical CS perspective.

2.4. Limitations of Angular Representations for Sparse Coding

We illustrate the limitations of sparse coding using a per-voxel angular representation on a 2D HARDI phantom dataset with $V=50 \times 50$ and $G = 64$ gradient directions (the same data is used in our experiments in Section 5). Specifically, we solve (5) with $\mathcal{R}(A) = 0$. (A nonzero choice of $\mathcal{R}(A)$ may improve reconstruction results but at a greater cost of sparsity.) For this setting, we choose angular basis Γ to be the well performing overcomplete spherical ridglet (SR) dictionary [39, 40, 59]. Figure 2 shows the ODF estimations (computed using the spherical wavelets [59]) from the sparse signal reconstruction for various sparsity levels compared to the ODFs estimated from the original signal, as well as close-ups of a region of interest (ROI) containing ODFs with complex crossings of 2, 3 and 4 fibers. We use 5 different values of λ which gives us global sparsity levels, $\|A\|_0/V$, of 0.246, 0.485, 1.11, 2.07, and 3.84 average atoms per voxel. As expected, when $\|A\|_0/V < 1$ (see top left/middle), many voxels are forced to zero (as indicated by yellow spheres in Figure 2). This is especially true for isotropic signals surrounding the fiber tracts. Also as expected, when $\|A\|_0/V \approx 1$, (see top right) many of the complex signals in the fiber crossing ROI are pushed to zero. This model requires close to $\|A\|_0/V = 4$ average atoms per voxel to achieve nearly accurate signal reconstruction (bottom middle). In fact, the actual number of coefficients per voxel to accurately represent typical dMRI data with angular bases is substantially higher. We illustrate this in Figure 3 which shows the number of atoms used to represent the HARDI signals in each voxel for the reconstructions in Figure 2. The bottom right image shows the ground truth number of fibers crossing in each voxel. This experiment demonstrates that voxels containing crossing fibers are forced to zero atoms when the average atoms per voxel are very sparse and tend to 6-12 atoms for accurate reconstruction when sparsity is increased. This is consistent with the reports of [39, 41] for the SR

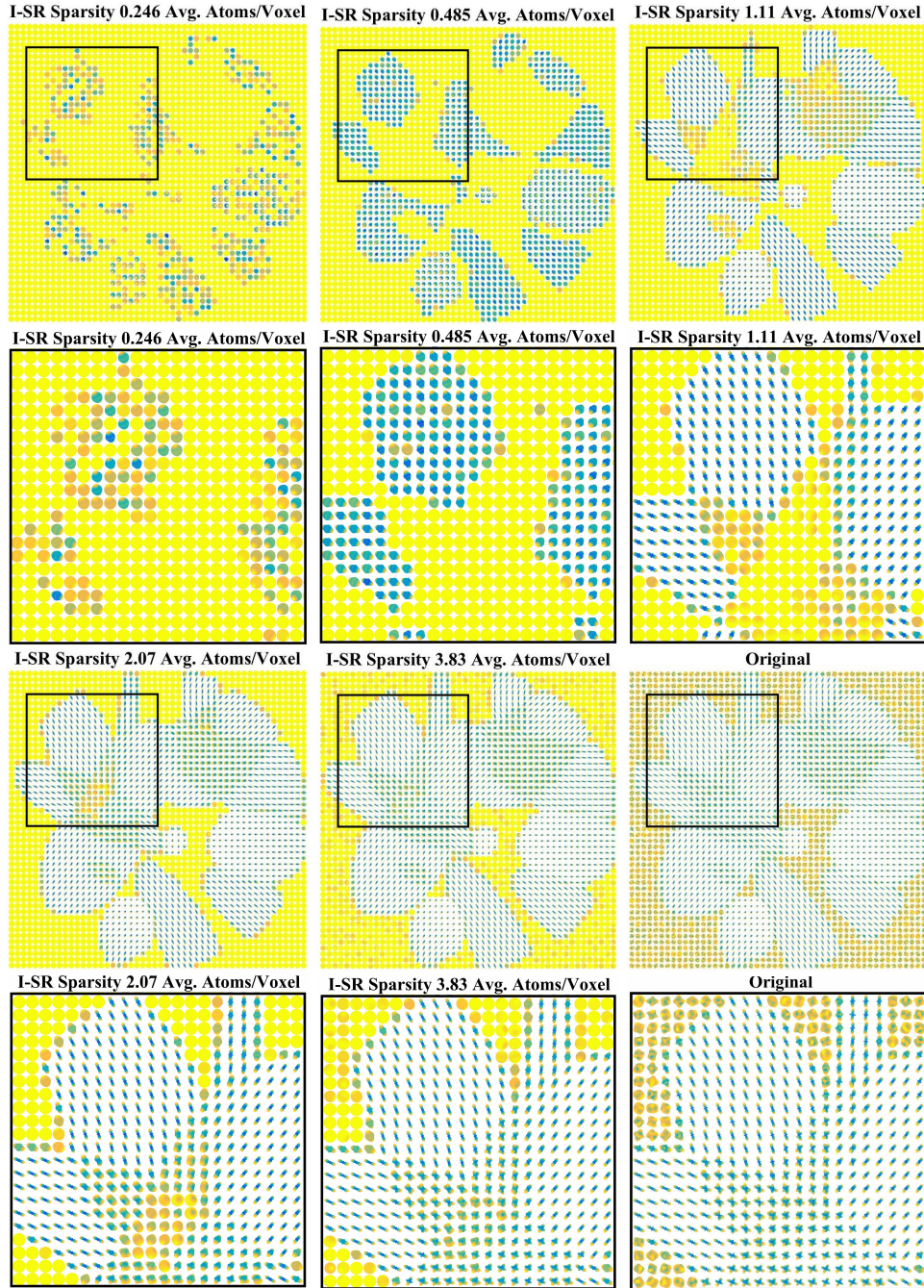


Figure 2: Qualitative demonstration of state-of-the-art sparse coding limitations (5) with the spherical ridgelets (SR) dictionary for 5 different global sparsity levels compared to the original signal (bottom right) with ROI closeups underneath. For high global sparsity levels (top left, middle), voxels with complex signals are forced to zero (yellow spheres). Regions with crossing fibers are unable to be accurately reconstructed even using up to global sparsity levels of 2.07 avg. atoms/voxel, showing limitation of state-of-the-art sparsity levels. The label I-SR refers to Identity-SR, explained in the next section.

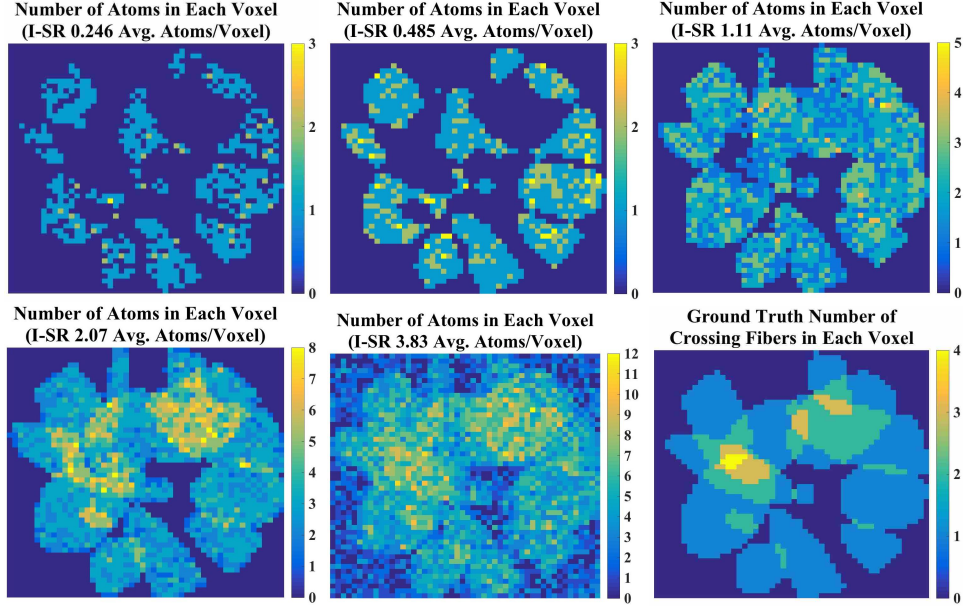


Figure 3: Number of atoms found in each voxel corresponding to the 5 levels global sparsity levels in Figure (2). The bottom right figure shows the ground truth number of fibers crossing in each voxel to illustrate the complexity of each angular signal in relation to how many atoms are needed to sparsely model them. Crossing fiber signals are either forced to zero for high global sparsity levels (see: top row) or require between 3-5 atoms for single fiber signals (see: avg. sparsity 1.11 and 2.07) and 6-12 for double and triple crossing fiber signals (see: avg. sparsity 3.83). The label I-SR refers to Identity-SR, explained in the experiments Section 5.

dictionary. In the following section, we present our global spatial-angular representation of dMRI with which we allow for the possibility to achieve accurate reconstruction with sparsity levels below the number of voxels, unachievable with an angular representation alone.

3. Joint Spatial-Angular dMRI Representation

In this work, to overcome the sparsity limits of an angular representation, we propose to model a dMRI signal $\mathcal{S} : \Omega \times \mathbb{R}^3 \rightarrow \mathbb{R}$ globally with a joint spatial-angular dictionary, say $\varphi(v, \vec{q})$, such that

$$\mathcal{S}(v, \vec{q}) = \sum_k c_k \varphi_k(v, \vec{q}) \quad (7)$$

with a single set of global coefficients $c = [c_k]$. A global dictionary allows us to find global representations with sparsity levels below the number of voxels without forcing some voxels to have zero signal. In fact, the sparsest possible representation would be the absolute limit of 1 nonzero coefficient c_k , and so we find ourselves in an unrestricted setting for global sparse coding. To set up the spatial-angular sparse coding problem, we let $s \in \mathbb{R}^{GV}$ be the vectorization of $\mathcal{S}(v, \vec{q})$ where for $v = 1 \dots V$ we stack the q -space signals, $s_v \in \mathbb{R}^G$, and $\Phi_k \in \mathbb{R}^{GV}$ be the vectorization $\varphi_k(v, \vec{q})$ to build the global dictionary $\Phi = [\Phi_1 \dots \Phi_{N_\Phi}] \in \mathbb{R}^{GV \times N_\Phi}$, with N_Φ

atoms. Then, to find a globally sparse c , we can solve the l_0 minimization problem:

$$c^* = \arg \min_c \frac{1}{2} \|\Phi c - s\|_2^2 \quad \text{s.t.} \quad \|c\|_0 \leq K, \quad (P0vec)$$

for global sparsity level K or the l_1 minimization problem:

$$c^* = \arg \min_c \frac{1}{2} \|\Phi c - s\|_2^2 + \lambda \|c\|_1, \quad (P1vec)$$

125 where $\lambda > 0$ is the sparsity trade-off parameter. However, typical dMRI contains on the order of $V \approx 100^3$ voxels each with $G \approx 100$ q -space measurements for a total of $100^4 = 100$ million signal measurements ($|s| \approx 10^8$). Since many sparse coding applications often utilize dictionaries that are over-redundant, this leads to a massive matrix Φ with 100^4 rows and over 100^4 columns ($|\Phi| \approx 10^{16}$). For some datasets, even committing Φ to memory is prohibitive. Therefore solving this large-scale global dMRI sparse coding problem 130 using traditional solvers like OMP to approximate $(P0vec)$ or ADMM and FISTA to solve $(P1vec)$, prove intractable.

To address this challenge, we introduce additional structure on the dictionary atoms by considering separable functions over Ω and \mathbb{R}^3 , namely a set of atoms of the form $\{\varphi_k(v, \vec{q})\} = \{\psi_j(v) \otimes \gamma_i(\vec{q})\}$, where $\{\psi_j(v)\}$ is a spatial basis for Ω and $\{\gamma_i(\vec{q})\}$ is an angular basis for \mathbb{R}^3 and \otimes is the Kronecker product. In discretized form for V voxels and G gradient directions, with $\Psi \in \mathbb{R}^{V \times N_\Psi}$ and $\Gamma \in \mathbb{R}^{G \times N_\Gamma}$, the matrix $\Phi = \Psi \otimes \Gamma$ is of the form:

$$s = \begin{pmatrix} s_1 \\ s_2 \\ \vdots \\ s_V \end{pmatrix} = \begin{pmatrix} \Psi_{1,1}\Gamma & \Psi_{1,2}\Gamma & \cdots & \Psi_{1,N_\Psi}\Gamma \\ \Psi_{2,1}\Gamma & \Psi_{2,2}\Gamma & \cdots & \Psi_{2,N_\Psi}\Gamma \\ \vdots & \vdots & \ddots & \vdots \\ \Psi_{V,1}\Gamma & \Psi_{V,2}\Gamma & \cdots & \Psi_{V,N_\Psi}\Gamma \end{pmatrix} \begin{pmatrix} c_1 \\ c_2 \\ \vdots \\ c_{N_\Psi N_\Gamma} \end{pmatrix} = \Phi c. \quad (8)$$

Figure 4 illustrates the Kronecker structure of spatial-angular atom Φ_k . We can see that by representing a dMRI signal with this type of global spatial-angular atom, one can model an entire region of the brain with as few as a single atom instead of angular atoms at every voxel.

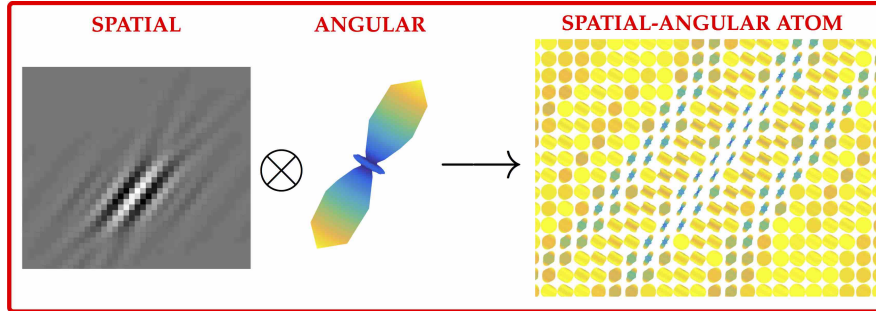


Figure 4: Example construction of a single spatial-angular basis atom Φ_k (right) by taking the Kronecker product of Ψ_j (left) and Γ_i (middle), i.e. $\Psi_j \otimes \Gamma_i = \Phi_k$. With this particular combination of spatial (curvelet [11]) and angular (spherical wavelet [59]) atoms, we can see that it may be possible to represent an entire fiber tract with very few spatial-angular atoms.

A motivating model for this separable structure for dMRI is as follows: first, as is traditionally done, the signal at each voxel $v \in \Omega$ is written as a linear combination of angular basis functions $\{\Gamma_i(\vec{q})\}$:

$$\mathcal{S}(v, \vec{q}) = \sum_{i=1}^{N_\Gamma} a_i(v) \Gamma_i(\vec{q}). \quad (9)$$

Then, we notice that each spherical coefficient $a_i(v)$ forms a 3D volume and so can be written as a linear combination of spatial basis functions $\{\Psi_j(v)\}$:

$$a_i(v) = \sum_{j=1}^{N_\Psi} c_{i,j} \Psi_j(v). \quad (10)$$

Combining (9) and (10) we arrive at our proposed separable spatial-angular dictionary

$$\mathcal{S}(v, \vec{q}) = \sum_{i=1}^{N_\Gamma} \sum_{j=1}^{N_\Psi} c_{i,j} \Psi_j(v) \Gamma_i(\vec{q}), \quad (11)$$

When stacking each s_v in a large vector, (11) results in the Kronecker product in (8), $s = (\Psi \otimes \Gamma)c$. Alternatively, when writing $S = [s_1, \dots, s_V]$ as a matrix, (11) results in the equivalent matrix form:

$$S = \Gamma C \Psi^\top. \quad (12)$$

135 Decomposing signals into Kronecker (or more general multi-tensor) structures has been well researched to increase algorithmic efficiency by reducing computations to the smaller, separate domains. Many research groups have exploited properties of the Kronecker product, when solving problem types of the form of (P0vec) and (P1vec) for computational efficiency of larger sparse coding [9], dictionary learning [26] and CS [19] applications. The work of [10] has applied multi-tensor sparse coding methods on dMRI data for
140 the application of fiber tract data compression. In particular, a Kronecker Orthogonal Matching Pursuit (Kron-OMP) [52] has been utilized to solve (P0vec). Although Kron-OMP becomes much more efficient than the classical OMP [60], the problem is not entirely separated into smaller domains, and the computationally expensive Φ matrix is still built explicitly. For large-scale problems like that of dMRI reconstruction, solving (P0vec) or (P1vec) even with a Kronecker structure dictionary remains largely intractable/expensive for
145 memory and computation time.

In contrast, we use the matrix form (12) which allows us to avoid the expensive uses of Φ and fully reduce computational complexity to the smaller separable basis domains of Γ and Ψ . In this paper we develop efficient algorithms to solve the completely separable spatial-angular sparse coding problems:

$$C^* = \arg \min_C \frac{1}{2} \|\Gamma C \Psi^\top - S\|_F^2 \text{ s.t. } \|C\|_0 \leq K \quad (P0mat)$$

and

$$C^* = \arg \min_C \frac{1}{2} \|\Gamma C \Psi^\top - S\|_F^2 + \lambda \|C\|_1. \quad (P1mat)$$

This becomes a general optimization to solve large-scale sparse coding problems with separable dictionaries and can also be extended to the tensor setting. As an important note, this matrix formulation is a generalization

of the voxel-wise angular sparse coding problem (5) in the special case of $\Psi = \mathbf{I}_V$, the $V \times V$ identity matrix, with $C \equiv A$. We use the identity as a choice for Ψ in the experiments of Section 5 when comparing the 150 performance of purely angular sparse coding with our proposed framework².

4. Efficient Kronecker Sparse Coding Algorithms

In what follows we present three novel adaptations of existing sparse coding algorithms for solving large-scale sparse coding problems with a Kronecker dictionary structure. These are Kronecker extensions of OMP (Section 4.2), ADMM (Section 4.3), and FISTA (Section 4.5). We compare these to existing Kronecker sparse 155 coding algorithms, a Kronecker OMP [52] (Section 4.1) as well as Kronecker Dual ADMM (Section 4.4), developed in our prior work [54] and derived in a new formulation for comparison in this paper. We compare these algorithms in terms of complexity for various types of bases in Section 4.6 and show experimental time comparisons in Section 5.

4.1. Kronecker OMP

160 To approximate a solution to the l_0 problem ($P0vec$), Orthogonal Matching Pursuit (OMP) [60] is a popular greedy algorithm that iteratively selects the atom that is most correlated with the signal, orthogonalizes it to the previously selected atoms by solving a least squares optimization, and selects the next atom that is most correlated with the resulting residual. For the case of a Kronecker structured basis, a Kronecker OMP (Kron-OMP) algorithm has been previously proposed [52, 9] that reduces computations of solving the 165 least squares subproblem in each iteration by exploiting properties of the Kronecker product. This form of Kron-OMP, however, represents the signal, coefficients, and basis atoms in vector form providing a solution to ($P0vec$). In Algorithm 1 we rewrite the Kron-OMP algorithm adapted to the structure of our problem, where $vec(\cdot)$ and $mat(\cdot)$ convert matrices to vectors and vice versa. The main complexity gain of Kron-OMP over the vector OMP is the separating of Γ and Ψ when computing the maximally correlated atoms with 170 the residual, $|\Gamma^\top R\Psi|$ (See Algorithm 1 Step 1) with complexity $O(N_\Gamma GV + GN_\Gamma N_\Psi)$ instead of computing $|\Phi^\top r|$ with complexity $O(N_\Gamma N_\Psi GV)$. The other gain is in solving the least squares problem (See Algorithm 1 Step 3) by exploiting properties of the Kronecker product ($A \odot B = [a_1 \otimes b_1, \dots, a_N \otimes b_N]$) to compute a rank-1 update. However, the only real improvement on complexity is in memory since Φ can be built atom by 175 atom from columns of Γ and Ψ instead of storing the entire matrix. The rank-1 update remains $O(k^2)$ for both vector and Kron-OMP. In the next section we present an alternative Kron-OMP algorithm that reduces complexity further by exploiting the full separability of the dictionary.

²Using $\Psi = \mathbf{I}_V$ identity with spherical ridgelets (SR) we adopt the notation I-SR for the dictionary used in the state-of-the-art illustration Figure 2 and Section 5.

Algorithm 1 Kron-OMP

Choose: K, ϵ .

Initialize: $k = 1, \mathcal{I}^0 = \emptyset, \mathcal{J}^0 = \emptyset, R_0 = S, s = \text{vec}(S)$.

while $k \leq K$ and error $> \epsilon$ **do**

- 1: $[i^k, j^k] = \arg \max_{[i,j]} |\Gamma^\top R_k \Psi|$;
- 2: $\mathcal{I}^k = [\mathcal{I}^{k-1}, i^k]; \mathcal{J}^k = [\mathcal{J}^{k-1}, j^k]; \mathcal{A}^k = (\mathcal{I}^k, \mathcal{J}^k)$;
- 3: $c_k = \arg \min_c \frac{1}{2} \|(\Gamma_{\mathcal{I}^k} \odot \Psi_{\mathcal{J}^k})c - s\|_2^2$;
- 4: $R_k = \text{mat}(s - (\Gamma_{\mathcal{I}^k} \odot \Psi_{\mathcal{J}^k})c_k)$;
- 5: $k \leftarrow k + 1$;

end while

Return: \mathcal{A}^K, c_K

4.2. Kronecker OMP with Projected Gradient Descent (PGD)

In what follows, we develop a novel form of Kronecker OMP which solves the separable ($P0mat$) instead of ($P0vec$). This allows us to reduce computation by not building columns of Φ and not repeating individual atoms of Γ or Ψ . Instead, indices of Γ and Ψ are updated only when they each have not been chosen before, fully exploiting the separability of the dictionary. Given the previous sets of respective of indices \mathcal{I}^{k-1} and \mathcal{J}^{k-1} , we update sets by following $\mathcal{I}^k = [\mathcal{I}^{k-1} i^k]$ if $i^k \notin \mathcal{I}^{k-1}$ and $\mathcal{I}^k = \mathcal{I}^{k-1}$ otherwise. Likewise, $\mathcal{J}^k = [\mathcal{J}^{k-1} j^k]$ if $j^k \notin \mathcal{J}^{k-1}$ and $\mathcal{J}^k = \mathcal{J}^{k-1}$ otherwise. With the selected indices, the size of C_k will be $|\mathcal{I}^k| \times |\mathcal{J}^k|$ instead of $k \times k$. To find for C_k , it seems natural to solve:

$$C_k = \arg \min_C \frac{1}{2} \|\Gamma_{\mathcal{I}^k} C \Psi_{\mathcal{J}^k}^\top - S\|_F^2. \quad (13)$$

But the solution C_k will contain possible nonzero coefficients that do not coincide with the chosen selection of indices since additional indices in all combinations of pairs between \mathcal{I}^k and \mathcal{J}^k will be updated in each iteration. This is problematic for the correctness of the algorithm when choosing the next single most correlated coefficient. Therefore we must enforce that these coefficients are zero:

$$C_k = \arg \min_C \frac{1}{2} \|\Gamma_{\mathcal{I}^k} C \Psi_{\mathcal{J}^k}^\top - S\|_F^2 \text{ s.t. } C_{i,j} = 0 \quad \forall (i,j) \in \mathcal{O}^k. \quad (14)$$

where $\mathcal{O}^k := \overline{(\mathcal{I}^k, \mathcal{J}^k)}$. To solve this problem, we can use projected gradient descent (PGD). The gradient of $f(C) = \frac{1}{2} \|\Gamma_{\mathcal{I}^k} C \Psi_{\mathcal{J}^k}^\top - S\|_F^2$ at iteration k is

$$\nabla f(C) = \Gamma_{\mathcal{I}^k}^\top \Gamma_{\mathcal{I}^k} C \Psi_{\mathcal{J}^k}^\top \Psi_{\mathcal{J}^k} - \Gamma_{\mathcal{I}^k}^\top S \Psi_{\mathcal{J}^k}. \quad (15)$$

To save on computation we precompute $\mathcal{G} = \Gamma^\top \Gamma$, $\mathcal{P} = \Psi^\top \Psi$, and $\hat{S} = \Gamma^\top S \Psi$ and can access their entries at each iteration: $\mathcal{G}_{\mathcal{I}^k, \mathcal{I}^k}, \mathcal{P}_{\mathcal{J}^k, \mathcal{J}^k}, \hat{S}_{\mathcal{I}^k, \mathcal{J}^k}$. Then we iteratively project the update in the gradient direction to the space of feasible solutions:

$$C^{t+1} = P_{\mathcal{O}^k}(C^t - \epsilon \nabla f(C^t)) \quad (16)$$

where the projection $P_{\mathcal{O}^k}$ sets all elements in \mathcal{O}^k to 0 and step-size ϵ is estimated each iteration using a line search. Once the procedure has converged, we compute the residual $R_k = S - \Gamma_{\mathcal{I}^k} C_k \Psi_{\mathcal{J}^k}^\top$. Then, for iteration 180 $k + 1$ we must find $(i^{k+1}, j^{k+1}) = \arg \max_{[i,j]} |\Gamma^\top R_k \Psi|$. To save significantly on computation we can instead use our precomputed \mathcal{G} and \mathcal{P} to instead find $\arg \max_{[i,j]} |\hat{R}_k|$, where $\hat{R}_k = \hat{S} - \mathcal{G}_{\mathcal{I}^k} C_k \mathcal{P}_{\mathcal{J}^k}^\top$ where $\mathcal{G}_{\mathcal{I}^k}, \mathcal{P}_{\mathcal{J}^k}$ respectively access the $\mathcal{I}^k, \mathcal{J}^k$ columns and all rows. Maintaining matrix forms throughout allows us to combine computing the residual and the next atoms for a large reduction in computation at each iteration k . Our proposed Kronecker OMP with projected gradient descent (Kron-OMP-PGD) is outlined in Algorithm 2.

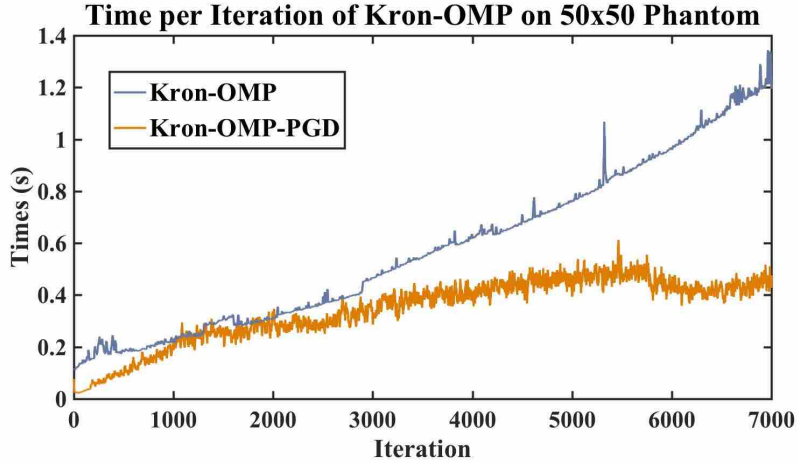


Figure 5: Comparison of time per iteration for Kron-OMP and the proposed Kron-OMP-PGD. The total time to choose $K = 7000 = 2.8V$ atoms for this $V = 50 \times 50$ slice of a phantom dataset, is 68 min for Kron-OMP and 40 min for Kron-OMP-PGD. We can see that as the number of atoms grows, the time per iteration of Kron-OMP continues to grow at a much higher rate than Kron-OMP-PGD.

185 We show a comparison of time per iteration for a small $V = 50 \times 50, G = 64$ phantom dataset in Figure 5. The steeper time increase for Kron-OMP is due to the fact that at iteration k there is a complexity of $O(k^2 + kGV)$ that comes from Steps 3 (rank-1 update) and 4 of Algorithm 1. On the other hand, Kron-OMP-PGD has complexity involving $|\mathcal{I}^k|, |\mathcal{J}^k| \leq k$ which are in practice significantly less than k . Even 190 though a PGD sub-routine must be performed at each iteration k , we found that by incorporating Nesterov acceleration with a line search, the time per iteration remains lower than Kron-OMP as the number of iterations k increases.

However, for dMRI data, typical sparsity levels are $K = O(V)$. So for $V \approx 100^3$ the number of iterations as well as the time per iteration of both Kron-OMP and Kron-OMP-PGD when k approaches K becomes astronomical. Even on a relatively small 3D phantom dataset of spatial size $V = 50 \times 50$, for example, one 195 iteration takes on the order of a few seconds which results in over 34 hrs for these greedy algorithms to reach 1 atom/voxel atoms ($K = V$). In this way, greedy algorithms such as OMP are not suitable for large-scale problems that require hundreds of thousands of iterations. Instead, optimizing the LASSO problem ($P1mat$) can be accomplished with significantly less iterations, as we examine in the following section.

Algorithm 2 Kron-OMP-PGD

Choose: $K, \epsilon_1, \epsilon_2$.

Precompute: $\hat{S} = \Gamma^\top S \Psi$, $\mathcal{G} = \Gamma^\top \Gamma$, $\mathcal{P} = \Psi^\top \Psi$.

Initialize: $k = 1$, $\mathcal{I}^0 = \emptyset$, $\mathcal{J}^0 = \emptyset$, $\hat{R}_0 = \hat{S}$.

while $k \leq K$ and error $> \epsilon_1$ **do**

- 1: $[i^k, j^k] = \arg \max_{[i, j]} |\hat{R}_k|$;
- 2: $\mathcal{I}^k = \mathcal{I}^{k-1} \cup i^k$; $\mathcal{J}^k = \mathcal{J}^{k-1} \cup j^k$; $\mathcal{A}^k = (\mathcal{I}^k, \mathcal{J}^k)$; $\mathcal{O}^k = \overline{\mathcal{A}^k}$;
- 3: $Z_{\mathcal{J}^{k-1}, \mathcal{I}^{k-1}}^1 = C_{k-1}$; $n_1 = 0$; $t = 1$;
- while** error $> \epsilon_2$ **do**

 - 1: $\delta = \text{linesearch}(Z^t)$;
 - 2: $C^{t+1} = P_{\mathcal{O}^k}(Z^t - \delta(\mathcal{G}_{\mathcal{I}^k, \mathcal{J}^k} Z^t \mathcal{P}_{\mathcal{J}^k, \mathcal{J}^k} - \hat{S}_{\mathcal{I}^k, \mathcal{J}^k}))$;
 - 4: $n_{t+1} = \frac{1}{2}(1 + \sqrt{1 + 4n_t^2})$;
 - 5: $Z^{t+1} = C^{t+1} + \frac{n_t - 1}{n_{t+1}}(C^{t+1} - C^t)$;
 - 6: $t \leftarrow t + 1$;

- end while**
- 4: $C_k = C^*$;
- 5: $\hat{R}_k = \hat{S} - \mathcal{G}_{\mathcal{I}^k} C_k \mathcal{P}_{\mathcal{J}^k}$;
- 6: $k \leftarrow k + 1$;

end while

Return: \mathcal{A}^K, C_K .

4.3. Kronecker ADMM

The Alternating Direction Method of Multipliers (ADMM) [8] is a popular method for solving the l_1 minimization problem (*P1vec*). However, its application in the case of a large dictionary Φ remains prohibitive, requiring computations involving $\Phi^\top s$ of order $O(GVN_\Gamma N_\Psi)$. Instead, we apply ADMM to the separable l_1 minimization problem (*P1mat*) to reduce computations by solving

$$\min_{C, Z} \frac{1}{2} \|\Gamma C \Psi^\top - S\|_F^2 + \lambda \|Z\|_1 \quad \text{s.t. } C = Z. \quad (17)$$

The augmented Lagrangian writes:

$$\mathcal{L}_\mu(C, Z, \mathcal{T}) = \frac{1}{2} \|\Gamma C \Psi^\top - S\|_F^2 + \lambda \|Z\|_1 + \langle \mathcal{T}, C - Z \rangle + \frac{\mu}{2} \|C - Z\|_F^2, \quad (18)$$

and:

$$\frac{\partial \mathcal{L}_\mu}{\partial C} = \Gamma^\top (\Gamma C \Psi^\top - S) \Psi + \mathcal{T} + \mu(C - Z) = 0 \quad (19)$$

$$\implies \Gamma^\top \Gamma C \Psi^\top \Psi + \mu C = \mu Z - \mathcal{T} + \Gamma^\top S \Psi := Q \quad (20)$$

To solve for C , we begin by taking the SVDs of Γ and Ψ . With $\Gamma = U_\Gamma \Sigma_\Gamma V_\Gamma^\top$ and $\Psi = U_\Psi \Sigma_\Psi V_\Psi^\top$, $\Gamma^\top \Gamma = V_\Gamma \Delta_\Gamma V_\Gamma^\top$ and $\Psi^\top \Psi = V_\Psi \Delta_\Psi V_\Psi^\top$, where U_Γ, U_Ψ are the matrices of eigenvectors and $\Delta_\Gamma = \Sigma_\Gamma^\top \Sigma_\Gamma$, $\Delta_\Psi = \Sigma_\Psi^\top \Sigma_\Psi$

are the diagonal matrices of eigenvalues for Γ and Ψ respectively. Then:

$$V_\Gamma \Delta_\Gamma V_\Gamma^\top C V_\Psi \Delta_\Psi V_\Psi^\top + \mu C = Q \quad (21)$$

$$\implies \Delta_\Gamma \tilde{C} \Delta_\Psi + \mu \tilde{C} = \tilde{Q} \quad (22)$$

where we introduced the notation $\tilde{X} = V_\Gamma^\top X V_\Psi$. Since Δ_Γ and Δ_Ψ are diagonal with elements δ_{Γ_i} and δ_{Ψ_j} , respectively, we can solve for \tilde{C} by:

$$\delta_{\Gamma_i} \tilde{C}_{i,j} \delta_{\Psi_j} + \mu \tilde{C}_{i,j} = \tilde{Q}_{i,j} \implies \tilde{C}_{i,j} = \frac{\tilde{Q}_{i,j}}{\delta_{\Gamma_i} \delta_{\Psi_j} + \mu} \quad (23)$$

To write this in matrix form we define $\Sigma_{\mu, i,j}^{-1} \triangleq 1/(\delta_{\Gamma_i} \delta_{\Psi_j} + \mu)$ and have $\tilde{C} = (\Sigma_{\mu}^{-1} \circ \tilde{Q})$ where \circ stands for element-wise matrix multiplication. Finally, we can recover $C = V_\Gamma \tilde{C} V_\Psi^\top$ and the complete update for C is:

$$C = V_\Gamma (\Sigma_{\mu}^{-1} \circ (V_\Gamma^\top Q V_\Psi)) V_\Psi^\top \quad (24)$$

200 where $Q = \mu Z - \mathcal{T} + \Gamma^\top S \Psi$. When minimizing \mathcal{L}_μ with respect to Z , we end up with the usual proximal operator of the l_1 norm that is given by the shrinkage operator, $\text{shrink}_\kappa(X) = \max(0, X - \kappa) - \max(0, -X - \kappa)$, applied element-wise to matrix X , giving $Z_{k+1} = \text{shrink}_{\lambda/\mu}(C_{k+1} + \mathcal{T}_k)$. Similarly with respect to \mathcal{T} , we have the usual Lagrange multiplier gradient ascent update $\mathcal{T}_{k+1} = \mathcal{T}_k + C_{k+1} - Z_{k+1}$. The formal updates for Kron-ADMM are presented in Algorithm 3. The update for C in (24) works well when Γ and Ψ are

Algorithm 3 Kron-ADMM (for undercomplete dictionaries)

Choose: μ, λ, ϵ .

Precompute: $V_\Gamma, \Delta_\Gamma, V_\Psi, \Delta_\Psi, \Sigma_{\mu}^{-1}$.

Initialize: $k = 0, Z_0 = \mathbf{0}, \mathcal{T}_0 = \mathbf{0}$.

while $\text{error} > \epsilon$ **do**

- 1: $Q = \Gamma^\top S \Psi + \mu Z_k - \mathcal{T}_k$;
- 2: $C_{k+1} = V_\Gamma (\Sigma_{\mu}^{-1} \circ (V_\Gamma^\top Q V_\Psi)) V_\Psi^\top$;
- 3: $Z_{k+1} = \text{shrink}_{\lambda/\mu}(C_{k+1} + \mathcal{T}_k)$;
- 4: $\mathcal{T}_{k+1} = \mathcal{T}_k + C_{k+1} - Z_{k+1}$;
- 5: $k \leftarrow k + 1$;

end while

Return: C^* .

205 under-complete and the eigen-decompositions of $\Gamma^\top \Gamma$ and $\Psi^\top \Psi$ are easily computable. However, dictionaries most commonly used for sparse coding and the application to CS are over-complete i.e. $G < N_\Gamma$ and $V < N_\Psi$ making these SVDs potentially expensive to compute. In the case of an over-complete Φ , for traditional vector ADMM, the matrix inversion lemma [8] is involved in order to compute SVDs of the smaller $\Phi \Phi^\top$ instead of $\Phi^\top \Phi$. In the following proposition, we derive the equivalent result for the update of C in (24).

Proposition 1. *For over-complete dictionaries Γ and Ψ , update (24) is equivalent to the more compact*

$$C = Q/\mu - \Gamma^\top U_\Gamma (\Sigma_{\mu}^{-1} \circ (U_\Gamma^\top \Gamma Q \Psi^\top U_\Psi)) U_\Psi^\top \Psi / \mu. \quad (25)$$

Proof. For over-complete dictionaries $\Gamma = U_\Gamma[\Sigma_\Gamma, \mathbf{0}]V_\Gamma^\top$ and $\Psi = U_\Psi[\Sigma_\Psi, \mathbf{0}]V_\Psi^\top$,

$$\Gamma^\top \Gamma = V_\Gamma \begin{pmatrix} \Delta_\Gamma & \mathbf{0} \\ \mathbf{0} & \mathbf{0} \end{pmatrix} V_\Gamma^\top \text{ and } \Psi^\top \Psi = V_\Psi \begin{pmatrix} \Delta_\Psi & \mathbf{0} \\ \mathbf{0} & \mathbf{0} \end{pmatrix} V_\Psi^\top.$$

For $G < i \leq N_\Gamma, V < j \leq N_\Psi, \delta_{\Gamma_i}, \delta_{\Psi_j} = 0$, so $\tilde{C}_{i,j} = \frac{\tilde{Q}_{i,j}}{\delta_{\Gamma_i} \delta_{\Psi_j} + \mu} = \frac{\tilde{Q}_{i,j}}{\mu}$. For $i \leq G$ and $j \leq V$, we can rewrite

$$\begin{aligned} \tilde{C}_{i,j} &= \frac{\tilde{Q}_{i,j}}{\delta_{\Gamma_i} \delta_{\Psi_j} + \mu} = \frac{\tilde{Q}_{i,j}}{\mu} - \frac{\delta_{\Gamma_i} \tilde{Q}_{i,j} \delta_{\Psi_j}}{\mu(\delta_{\Gamma_i} \delta_{\Psi_j} + \mu)} = \frac{\tilde{Q}_{i,j}}{\mu} - \frac{\sigma_{\Gamma_i}^2 \tilde{Q}_{i,j} \sigma_{\Psi_j}^2}{\mu(\delta_{\Gamma_i} \delta_{\Psi_j} + \mu)} \\ &= \frac{\tilde{Q}_{i,j}}{\mu} - \sigma_{\Gamma_i} \frac{\sigma_{\Gamma_i} \tilde{Q}_{i,j} \sigma_{\Psi_j}}{\mu(\delta_{\Gamma_i} \delta_{\Psi_j} + \mu)} \sigma_{\Psi_j} \\ \implies \tilde{C} &= \tilde{Q}/\mu - \Sigma_\Gamma^{-1} \circ (\Sigma_\Gamma \tilde{Q} \Sigma_\Psi^\top) \Sigma_\Psi / \mu \\ C &= Q/\mu - V_\Gamma \Sigma_\Gamma^{-1} \circ (\Sigma_\Gamma V_\Gamma^\top Q V_\Psi \Sigma_\Psi^\top) \Sigma_\Psi V_\Psi^\top / \mu \\ C &= Q/\mu - \Gamma^\top U_\Gamma (\Sigma_\mu^{-1} \circ (U_\Gamma^\top \Gamma Q \Psi^\top U_\Psi)) U_\Psi^\top \Psi / \mu \end{aligned}$$

210

□

Letting $\Gamma' = U_\Gamma^\top \Gamma$ and $\Psi' = U_\Psi^\top \Psi$, which can be precomputed, we have a final efficient update

$$C = Q/\mu - \Gamma'^\top (\Sigma_\mu^{-1} \circ (\Gamma' Q \Psi'^\top)) \Psi' / \mu \quad (26)$$

This allows us to compute the SVDs of $\Gamma \Gamma^\top$ and $\Psi \Psi^\top$ instead of the larger $\Gamma^\top \Gamma$ and $\Psi^\top \Psi$ and work with smaller matrices within each iteration. We present Kron-ADMM for over-complete dictionaries in Algorithm 4.

Algorithm 4 Kron-ADMM (for overcomplete dictionaries)

Choose: μ, λ, ϵ .

Precompute: $U_\Gamma, \Delta_\Gamma, U_\Psi, \Delta_\Psi, \Gamma', \Psi', \Sigma_\mu^{-1}$.

Initialize: $k = 0, Z_0 = \mathbf{0}, \mathcal{T}_0 = \mathbf{0}$.

while $\text{error} > \epsilon$ **do**

- 1: $Q = \Gamma^\top S \Psi + \mu Z_k - \mathcal{T}_k$;
- 2: $C_{k+1} = Q/\mu - \Gamma'^\top (\Sigma_\mu^{-1} \circ (\Gamma' Q \Psi'^\top)) \Psi' / \mu$;
- 3: $Z_{k+1} = \text{shrink}_{\lambda/\mu}(C_{k+1} + \mathcal{T}_k)$;
- 4: $\mathcal{T}_{k+1} = \mathcal{T}_k + C_{k+1} - Z_{k+1}$;
- 5: $k \leftarrow k + 1$;

end while

Return: C^* .

4.4. Kronecker Dual ADMM

As an alternative to ADMM, Dual ADMM, which applies ADMM to the dual of $l1$ problem (*P1vec*), has been shown to be more efficient than ADMM for over-complete dictionaries [23] by allowing one to compute SVDs of the more affordable $\Phi \Phi^\top$ instead of $\Phi^\top \Phi$. In our previous work [54] we proposed a Kronecker Dual

ADMM (Kron-DADMM) that efficiently solves the spatial-angular sparse coding problem. Below, we give an alternative derivation of this algorithm directly based on the matrix formulation of $(P1mat)$. The dual of $(P1mat)$ is:

$$\max_A -\frac{1}{2} \|A\|_F^2 + A^\top S \quad \text{s.t.} \quad \|\Gamma^\top A\Psi\|_\infty \leq \lambda. \quad (27)$$

To apply ADMM to this optimization problem, we replace $\Gamma^\top A\Psi$ with auxiliary variable \mathcal{V} and add the additional constraint $\Gamma^\top A\Psi - \mathcal{V} = 0$ to get:

$$\max_{A, \mathcal{V}} -\frac{1}{2} \|A\|_F^2 + A^\top S \quad \text{s.t.} \quad \|\mathcal{V}\|_\infty \leq \lambda \quad \text{and} \quad \mathcal{V} = \Gamma^\top A\Psi. \quad (28)$$

Then the augmented Lagrangian is

$$\mathcal{L}_\eta(A, \mathcal{V}, C) = -\frac{1}{2} \|A\|_F^2 + A^\top S + \langle C, \mathcal{V} - \Gamma^\top A\Psi \rangle + \frac{\eta}{2} \|\mathcal{V} - \Gamma^\top A\Psi\|_F^2 + \delta_\lambda(\mathcal{V}) \quad (29)$$

where

$$\delta_\lambda(\mathcal{V}) = \begin{cases} 0 & \text{if } \|\mathcal{V}\|_\infty \leq \lambda \\ \infty & \text{if } \|\mathcal{V}\|_\infty > \lambda \end{cases}. \quad (30)$$

The Lagrange multiplier C corresponds to the primal variable C in $(P1mat)$, our variable of interest. Then

$$\frac{\partial \mathcal{L}_\eta(A, \mathcal{V}, C)}{\partial A} = -A + S - \Gamma C \Psi^\top + \eta \Gamma (\mathcal{V} - \Gamma^\top A\Psi) \Psi^\top = 0 \quad (31)$$

$$\implies A + \eta \Gamma \Gamma^\top A \Psi \Psi^\top = S - \Gamma(C - \eta \mathcal{V}) \Psi^\top := P. \quad (32)$$

Now with eigen-decompositions $\Gamma \Gamma^\top = U_\Gamma \Delta_\Gamma U_\Gamma^\top$ and $\Psi \Psi^\top = U_\Psi \Delta_\Psi U_\Psi^\top$ and letting $\tilde{X} = U_\Gamma^\top X U_\Psi$,

$$A + \eta U_\Gamma \Delta_\Gamma U_\Gamma^\top A U_\Psi \Delta_\Psi U_\Psi^\top = P \quad (33)$$

$$\implies \tilde{A} + \eta \Delta_\Gamma \tilde{A} \Delta_\Psi = \tilde{P}. \quad (34)$$

Then, \tilde{A} can be found element-wise by:

$$\tilde{A}_{i,j} + \eta \delta_{\Gamma_i} \tilde{A}_{i,j} \delta_{\Psi_j} = \tilde{P}_{i,j} \implies \tilde{A}_{i,j} = \frac{\tilde{P}_{i,j}}{1 + \eta \delta_{\Gamma_i} \delta_{\Psi_j}}. \quad (35)$$

Defining $\Sigma_{\eta i,j}^{-1} \triangleq 1/(1 + \eta \delta_{\Gamma_i} \delta_{\Psi_j})$, the update is $\tilde{A} = \Sigma_\eta^{-1} \circ \tilde{P}$. As shown in [23] we can keep the update in terms of \tilde{A} instead of A since the variable we are interested in is C . We can then precompute $S' = \Gamma'^\top S \Psi'$, $\Gamma' = U_\Gamma^\top \Gamma$ and $\Psi' = U_\Psi^\top \Psi$. The updates of \mathcal{V} and C are as in [54] and presented in Algorithm 5, where $P_\lambda^\infty(X)$ sets all entries of matrix X that are greater than λ to λ .

Algorithm 5 Kron-DADMM

Choose: η, λ, ϵ .
 Precompute: $S', \Gamma', \Psi', \Sigma_\eta^{-1}$.
 Initialize: $k = 0, C_0 = 0, \mathcal{V}_0 = 0$.
while Duality Gap $> \epsilon$ **do**
 1: $\tilde{A}_{k+1} = \Sigma_\eta^{-1} \circ (S' - \Gamma'(C_k - \eta_k \mathcal{V}_k) \Psi'^\top)$;
 2: $\mathcal{V}_{k+1} = P_\lambda^\infty(\frac{1}{\eta} C_k + \Gamma'^\top \tilde{A}_{k+1} \Psi')$;
 3: $C_{k+1} = \text{shrink}_{\lambda\eta}(C_k + \eta \Gamma'^\top \tilde{A}_{k+1} \Psi')$;
 4: $k \leftarrow k + 1$;
end while
 Return: C^* .

4.5. Kronecker FISTA

The Fast Iterative Thresholding Algorithm (FISTA) [6] is another well-known method for solving LASSO. However, just as before, applying FISTA to $(P1vec)$ for large-scale dMRI data is largely intractable. So here we adapt FISTA to $(P1mat)$ in order to exploit the separability of our spatial-angular basis. FISTA is a proximal gradient descent

$$C_{k+1} = \text{shrink}_{\lambda/L}(C_k - \nabla f(C_k)/L), \quad (36)$$

where the proximal operator is the soft-thresholding shrinkage operator associated with the $l1$ norm and $1/L$ is a chosen step size. The gradient is simply computed as:

$$\nabla f(C) = \Gamma^\top (\Gamma C \Psi^\top) \Psi - \Gamma^\top S \Psi. \quad (37)$$

To help speed convergence, we invoke a line search subroutine to update L at each iteration in addition to the usual Nesterov acceleration. By [6], FISTA will converge for any L greater than the Lipschitz constant of ∇f which can be estimated by bounding

$$\|\nabla f(C) - \nabla f(\bar{C})\|_F = \|\Gamma^\top \Gamma(C - \bar{C}) \Psi^\top \Psi\|_F \leq \lambda_{\max}^\Gamma \lambda_{\max}^\Psi \|C - \bar{C}\|_F \quad (38)$$

where λ_{\max}^Γ and λ_{\max}^Ψ are the maximum eigenvalues of $\Gamma^\top \Gamma$ and $\Psi^\top \Psi$ respectively. Therefore we initialize
 220 $L = \lambda_{\max}^\Gamma \lambda_{\max}^\Psi$. The Kronecker FISTA (Kron-FISTA) is presented in Algorithm 6. This natural Kronecker extension to FISTA has also been recently presented in [48], but has not been adapted and tested on data of our scale.

Algorithm	Standard	Kronecker
OMP	$k^2 + kGV + GVN_{\Gamma}N_{\Psi}$	$k^2 + kGV + GVN_{\Gamma} + VN_{\Gamma}N_{\Psi}$
OMP-PGD	–	$TG \mathcal{I}^k \mathcal{J}^k + TGV \mathcal{J}^k + \mathcal{J}^k N_{\Gamma}N_{\Psi}$
ADMM	$(GV)^2N_{\Gamma}N_{\Psi} + GV(N_{\Gamma}N_{\Psi})^2$	$(GN_{\Gamma}N_{\Psi} + GVN_{\Psi}) + GV$
DADMM	$(GV)^2N_{\Gamma}N_{\Psi}$	$(GN_{\Gamma}N_{\Psi} + GVN_{\Psi}) + GV$
FISTA	$(N_{\Gamma}N_{\Psi})^2 + GVN_{\Gamma}N_{\Psi}$	$(GN_{\Gamma}N_{\Psi} + GVN_{\Psi})$

Table 2: Comparison of algorithms complexity at iteration k . For Kron-OMP-PGD, T is the number of sub-iterations of PGD.

Algorithm 6 Kron-FISTA

Choose: ϵ .
 Precompute: $\hat{S} = \Gamma^{\top}S\Psi$
 Initialize: $Z_1 = C_0 = \mathbf{0}$, $n_1 = 1$, $L = \lambda_{\max}^{\Gamma}\lambda_{\max}^{\Psi}$.
while error $> \epsilon$ **do**
 1: $L = \text{linesearch}(Z_k)$;
 2: $\nabla f(Z_k) = \Gamma^{\top}(\Gamma Z_k \Psi^{\top})\Psi - \hat{S}$;
 3: $C_k = \text{shrink}_{\lambda/L}(Z_k - \nabla f(Z_k)/L)$;
 4: $n_{k+1} = \frac{1}{2}(1 + \sqrt{1 + 4n_k^2})$;
 5: $Z_{k+1} = C_{k+1} + \frac{n_k - 1}{n_{k+1}}(C_{k+1} - C_k)$;
 6: $k \leftarrow k + 1$;
end while
 Return: C^* .

4.6. Complexity Analysis

To evaluate the efficiency of each algorithm and the gains of Kronecker separability compared to the original algorithms we summarize the complexity of each algorithm for general Ψ and Γ in Table 2. We notice that for classical l_1 algorithms have complexity on the order of the size of the Φ matrix, including terms that multiply all four dimensions $GVN_{\Gamma}N_{\Psi}$. When applying the Kronecker l_1 algorithms, the complexity is reduced to a summation that includes only 3 of the dimensions GVN_{Ψ} , a reduction on the order of N_{Γ} (≈ 200 for some of our dictionary choices). We compare the Kronecker l_1 algorithms empirically in Section 5 to identify which is fastest for our regime. Next we address the fact that the dimensions of $\Gamma \in \mathbb{R}^{G \times N_{\Gamma}}$ and $\Psi \in \mathbb{R}^{V \times N_{\Psi}}$ will be orders of magnitude different since $G \approx 100$ and $V \approx 100^3$. We consider a few specific assumptions on the structure of spatial dictionary Ψ which can decrease the complexity and simplify computations of some of the proposed algorithms:

Ψ Tight Frame. In the case that Ψ is a tight frame, *i.e.* $\Psi\Psi^{\top} = \mathbf{I}$, which is commonly an assumption in CS theorems, our method can still be simplified. In Kron-ADMM (overcomplete) and Kron-DADMM, we may avoid the SVD of $\Psi\Psi^{\top}$ and respective updates (22) and (34) can be simplified.

Ψ Fast Transform. In the case that Ψ corresponds to a well-studied transform such as wavelets, curvelets, etc., fast transform implementations can be utilized to reduce complexity further. For the case of FISTA, for example, matrix multiplications of $\Gamma^\top(\Gamma Z_k \Psi^\top)\Psi$ (See Algorithm 6 Step 2) involve fast transform reconstructions (Ψ^\top) of each DWI (ΓZ_k) and then deconstructions (Ψ) which we parallelize over all DWI in our implementation.

Ψ Orthonormal. In the case that Ψ is orthonormal, *i.e.* $\Psi^\top \Psi = \Psi \Psi^\top = I$ then (*P1mat*) can be simplified to (5) after noticing:

$$\|\Gamma C \Psi^\top - S\|_F^2 = \|\Gamma C \Psi^\top \Psi - S \Psi\|_F^2 = \|\Gamma C - \hat{S}\|_F^2. \quad (39)$$

This optimization can be solved using traditional methods after precomputing $\hat{S} = S \Psi$.

Ψ Separable Tensor Product. In the case that Ψ can be separated into a 3D tensor product $\Psi = \Psi_x \otimes \Psi_y \otimes \Psi_z$, the complexity of multiplication can be simplified by another degree, in the same vein as the decrease in complexity we gained from using $\Phi = \Psi \otimes \Gamma$. In this case, instead of the matrix multiplication, $S = \Gamma C \Psi^\top$ can be written using n-mode products of tensors $\mathcal{S} = \mathcal{C} \times_x \Psi_x \times_y \Psi_y \times_z \Psi_z \times_q \Gamma$. Furthermore, if we consider DSI acquisition where q -space measurements are acquired in a grid over \mathbb{R}^3 , and assume we can represent these measurements over a separable basis over each dimension, then we can take $\Gamma = \Gamma_{q_x} \otimes \Gamma_{q_y} \otimes \Gamma_{q_z}$ and Φ becomes a 6-tensor.

250 5. Experiments

5.1. Data

In this paper the type of data we experiment on is single-shell HARDI, though as we emphasized earlier, our framework and algorithms can be applied to any type of dMRI acquisition protocol with specific choice of angular basis Γ . We experimented on a phantom and real HARDI brain dataset. We applied our methods on the ISBI 2013 HARDI Reconstruction Challenge Phantom dataset, a $V = 50 \times 50 \times 50$ volume consisting of 20 phantom fibers crossing intricately within an inscribed sphere, measured with $G = 64$ gradient directions (SNR = 30). Our initial experiments test on a 2D 50×50 slice of this data for simplification. The real HARDI brain dataset consists of a $V = 112 \times 112 \times 65$ volume with $G = 127$ gradient directions. We conducted experiments on the core white matter brain region of size $V = 60 \times 60 \times 30$.

260 5.2. Kronecker Algorithm Comparison

In this section we compare the computational time performance of each of the proposed Kronecker LASSO algorithms, Kron-ADMM, Kron-DADMM, and Kron-FISTA on a 2D 50×50 slice of phantom data for various values of λ using Haar-SR. For our experiment, we ran Kron-FISTA until a very small error of 10^{-8} was reached. The objective value obtained was then taken to be a rough ground truth minimum. We then tested each of Kron-ADMM, Kron-DADMM, and Kron-FISTA and recorded the time it took to reach a relative error of 10^{-4} from the known minimum. Figure 6 reports the objective value descent of each algorithm

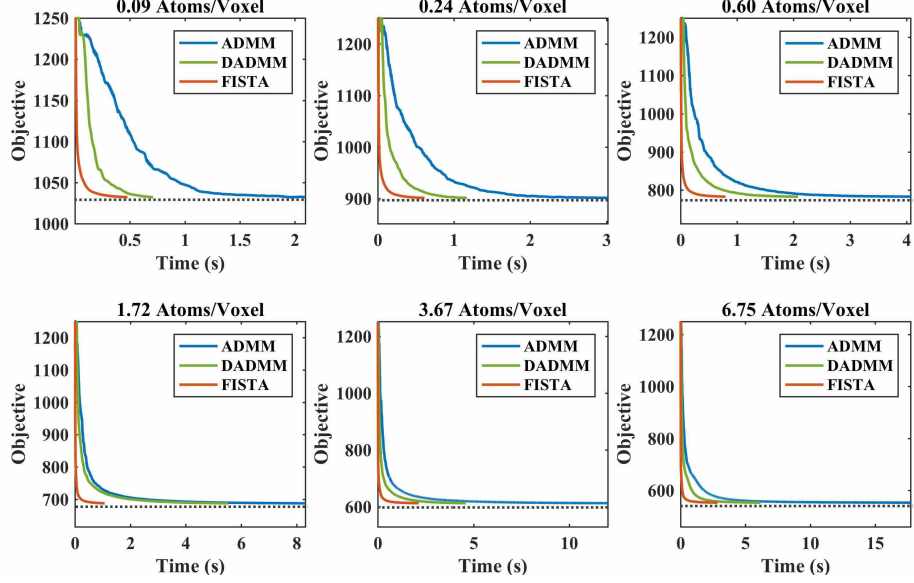


Figure 6: Comparison of time for completion of Kron-ADMM, Kron-DADMM, and Kron-FISTA on a 2D 50×50 phantom HARDI data using Haar-SR for various sparsity levels. Kron-FISTA consistently reaches the known minimum objective in the least amount of time.

for various sparsity levels associated to choices of λ . For our experiments, Kron-FISTA appears to be the fastest algorithm in all cases, followed by Kron-DADMM. The superior performance of DADMM over ADMM is consistent with the findings of [23]. With these results, we henceforth use Kron-FISTA for subsequent experiments.

5.3. Choice of Spatial-Angular Dictionaries

In this work we consider fixed spatial and angular dictionaries. For the choice of angular dictionary Γ , we consider the over-complete Spherical Ridgelet (SR) basis [59], which has been shown to sparsely model HARDI signals while ODFs are sparsely modeled with spherical wavelets (SW) counterparts (featured as the angular atom in Figure 4). With order $L = 2$ and 4, the SR dictionary contains $N_\Gamma = 210$ and $N_\Gamma = 1169$ atoms, respectively. We used both amounts of atoms for the small 2D 50×50 phantom dataset and found roughly identical results suggesting that order $L = 2$ supply enough atoms if the number of gradients is below 210. This reduces computation significantly. In our previous work [54] we compared the performance of SR with the spherical harmonic (SH) basis which has been shown in prior work [59] to not exude sparse signals and so we do not repeat this comparison in the current work.

For the choice of spatial dictionary Ψ , the spatial wavelet transform is one popular basis for which natural images and structural MRI volumes are considered sparse. In our previous work [54] we compared the performance of Daubechies wavelets and Haar wavelets and concluded that Daubechies resulted in a boundary smoothing between isotropic and anisotropic regions which was not indicative of the more abrupt boundaries that real HARDI data exhibits. Haar outperformed Daubechies in reconstruction error due in

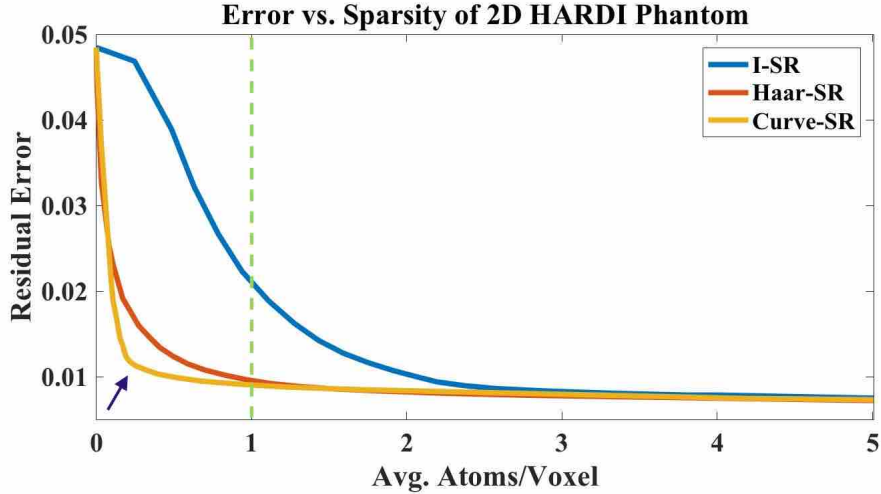


Figure 7: Quantitative results of residual error vs. global sparsity levels for I-SR, Haar-SR, and Curve-SR on 2D phantom data for various values of λ . Curve-SR out performs Haar-SR for low sparsity levels while I-SR has very high relative reconstruction error. The reconstruction of I-SR data points are displayed in Figure 2 and Haar-SR/Curve-SR in Figure 8. Our finding of I-SR requiring 6-8 atoms per voxel for accurate reconstruction is consistent with previous findings [39, 41].

part by HARDI’s more rigid boundaries and piece-wise consistencies, a spatial feature which have been reason for using total-variation penalties in many other reconstruction methods. For this reason, we do not consider Daubechies in this work. In addition to Haar, we consider the spatial curvelets dictionary [11] (featured as the spatial atom in Figure 4) which, in addition to variations in position and scale, offers directional variations
290 which may be useful for sparsely modeling the naturally directional HARDI fiber tracts regions. An important criteria for our spatial basis choices is that these spatial bases are tight frames which has important theoretical implications for CS and offers computational simplification (as discussed in Section 4.6). They additionally have fast transform implementations which also reduce computational complexity. Finally, to compare our formulation to state-of-the-art voxel-wise angular sparse coding, we can simply choose Ψ to be the $V \times V$
295 identity I_V . For simplification, we use a spatial-angular Ψ - Γ labeling: Haar-SR, Curve-SR, I-SR for Haar wavelets, curvelets, and the identity, respectively, for the spatial domain with SR for the angular domain.

5.4. Sparsity Results

In this section we compare our spatial-angular sparse coding, to state-of-the-art angular sparse coding to show drastic decreases in global sparsity while maintaining accurate reconstruction. The first experiment is
300 tested on the 50×50 phantom data slice. We ran Kron-FISTA for various values of λ for Haar-SR, Curve-SR and I-SR. In Figure 7 we show the results of residual reconstruction error $\frac{1}{GV} \|S^* - S_{orig}\|_F$ vs. global sparsity levels in terms of avg. number of atoms per voxel ($\|C^*\|_0/V$). The ideal reconstruction will have a very low residual error at a very high sparsity, i.e. low number of avg. atoms/voxel, occupying the lower left-hand corner of our plot. We can see that in this range, Curve-SR outperforms Haar-SR while I-SR is unable to perform at

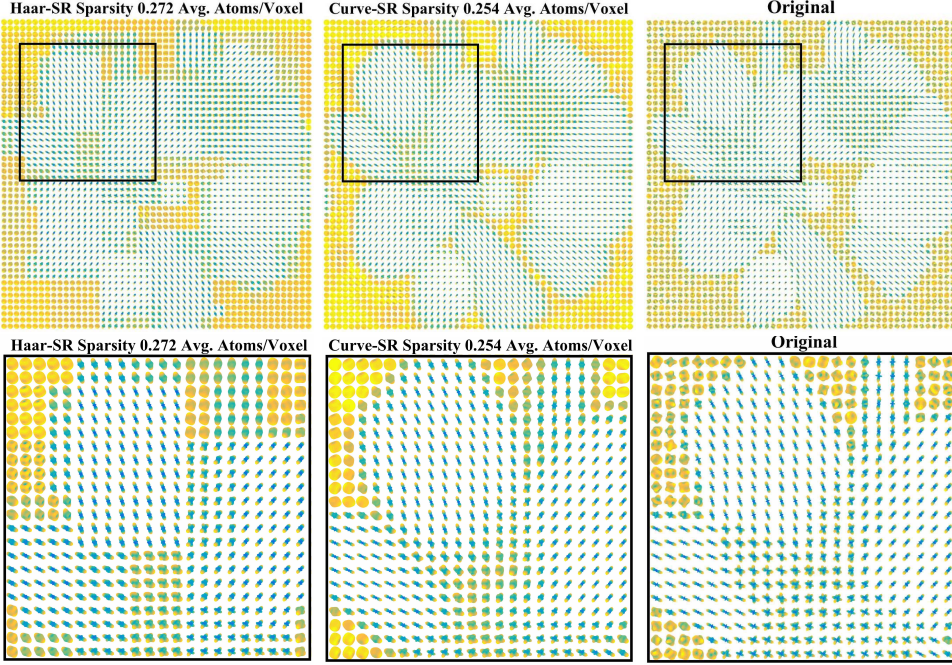


Figure 8: Results of the proposed spatial-angular sparse coding using Kron-FISTA for Haar-SR and Curve-SR at very high sparsity level of ~ 0.25 avg. atoms/voxel compared to original signal. Curve-SR outperforms Haar-SR in this high sparsity range due to its additional directionality. We can see a much better reconstruction of compared to the state-of-the-art in Figure 2. This clearly shows that we can achieve accurate reconstruction with global sparsity levels well below 1 atom/voxel.

305 this level. Reconstruction of I-SR for various sparsity levels are visualized in Figure 2. In comparison, Figure 8 displays the sparse reconstruction of Haar-SR and Curve-SR, each with global sparsity levels of around 0.25 avg. atoms/voxel. Notice that Curve-SR leads to a somehow smoother and more accurate reconstruction than the expectedly boxy reconstruction of Haar-SR at this very high sparsity level. Still, in both cases, the proposed joint spatial-angular sparse coding can reconstruct accurate signals with much fewer number of
310 atoms than angular sparse coding, which as seen again from Figure 2 can be achieved with an average of around 4 atoms per voxel. More strikingly, in cases of high signal complexity for crossing fibers, the sparse code requires on the order of 6-12 atoms per voxel (see Figure 3). We repeated this same analysis on real HARDI data. Figure 9 presents the reconstruction error vs. sparsity results for I-SR, Haar-SR, and Curve-SR showing again that curvelets outperforms Haar for high sparsity levels in the range of 0.5-2 avg. atoms/voxel.
315 As expected and consistent with our phantom data experiment, the state-of-the-art I-SR has comparable reconstruction error in the range of 6-8 avg. atoms/voxel. Figure 10 shows the quality of reconstruction of I-SR, Haar-SR, and Curve-SR compared the original signal for the high sparsity level of ~ 1 avg. atom/voxel. Haar-SR presents boxy regions while Curve-SR maintains a smoother reconstruction with a preservation of smaller detailed fiber tract regions. In contrast, the state-of-the-art I-SR is unable to model intricate
320 fiber regions and is forced to set most voxels to zero atoms. All in all, we can see that using our proposed

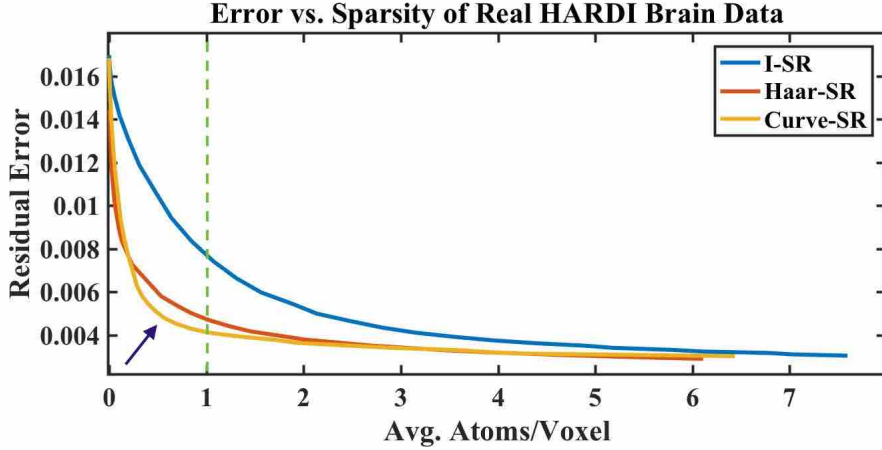


Figure 9: Global sparsity comparison of Haar-SR and Curve-SR with the state-of-the-art I-SR. The curvelets provide a good reconstruction error with the sparsest number of atoms, in the range of 0.5 to 2 avg. atoms/voxel. The state-of-the-art error is much larger in this sparsity range and only comparable in the predicted range of 6-8 avg. atoms/voxel, consistent with the previously reported [39, 41] for I-SR.

method, we can achieve much higher sparsity levels than the state-of-the-art, and accurate reconstructions using less than 1 atom/voxel. In terms of efficiency, Kron-FISTA was completed on the real HARDI data of size $V = 60 \times 60 \times 30$, $G = 127$ in 1.5 hours for our sparsity level of interest using the fast 3D wavelet transform implemented in MATLAB.

³²⁵ **6. Discussion and Conclusion**

In this work, we have demonstrated that by using a joint spatial-angular dictionary, we can obtain accurate HARDI reconstruction with global sparsity levels of less than one atom per voxel, surpassing the limitations of state-of-the-art angular representations. This provides a new general reconstruction framework to achieve sparser dMRI representations than previously possible with optimal choices of spatial and angular dictionaries.

³³⁰ In particular, we have shown promising sparsity results for HARDI from the combination of curvelet (spatial) and spherical ridgelet (angular) dictionaries, but other spatial and angular dictionaries may be chosen for other dMRI protocols like DSI or MS-HARDI. In future work, we aim to further optimize sparsity levels by learning a joint spatial-angular dictionary directly from dMRI data.

Furthermore, to efficiently solve this large-scale global sparse coding problem, we have proposed three ³³⁵ novel extensions of popular sparse coding algorithms for the Kronecker dictionary setting. All strategies improve upon previously proposed algorithms by explicitly exploiting the separability of the dictionary and each may be beneficial depending on the problem regime and size of data. For our large-scale HARDI data, Kron-FISTA was the leader in speed. In future work, we will investigate other efficient active set methods such as the recent ORacle Guided Elastic Net (ORGEN) [70].

³⁴⁰ In addition to sparse coding, our spatial angular representation may have novel applications in other areas

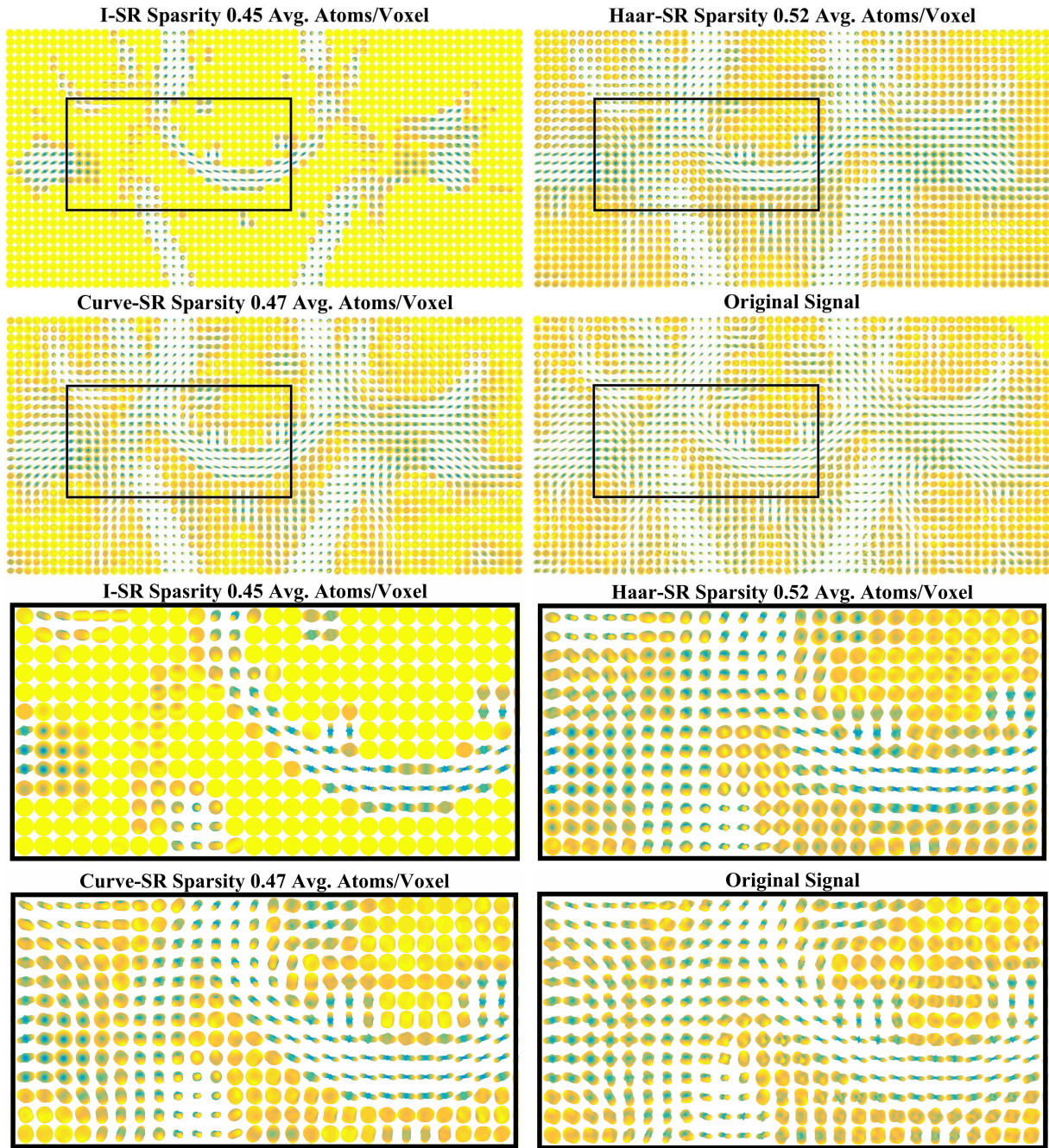


Figure 10: Results of proposed spatial-angular sparse coding on real HARDI brain data using Kron-FISTA for I-SR, Haar-SR and Curve-SR at very high sparsity level of ~ 0.5 avg. atoms/voxel compared to original signal. Curve-SR outperforms Haar-SR in this high sparsity range due to its directionality. The state-of-the-art I-SR is unable to compete at this sparsity level.

of dMRI processing such as denoising, feature extraction, global ODF non-negativity, fiber tract segmentation, and tractography. However, our main application for spatial-angular sparse coding framework is the promising improvements of acquisition acceleration of dMRI through CS. We aim to reduce signal measurements jointly in k - and q -space below the state-of-the-art by naturally incorporating our joint spatial-angular sparsifying 345 dictionary within a unified (k, q) -CS framework.

Acknowledgements. This work supported by Johns Hopkins University startup funds.

References

- [1] I. B. Alaya, M. Jribi, F. Ghorbel, and T. Kraiem. A Novel Geometrical Approach for a Rapid Estimation of the HARDI Signal in Diffusion MRI. In *International Conference on Image and Signal Processing*, pages 253–261. Springer, 2016.
- 350 [2] R. Aranda, A. Ramirez-Manzanares, and M. Rivera. Sparse and Adaptive Diffusion Dictionary (SADD) for recovering intra-voxel white matter structure. *Medical Image Analysis*, 26(1):243–255, 2015.
- [3] A. Auría, A. Daducci, J.-P. Thiran, and Y. Wiaux. Structured sparsity for spatially coherent fibre orientation estimation in diffusion MRI. *NeuroImage*, 115:245–255, 2015.
- 355 [4] S. Awate and E. DiBella. Compressed sensing HARDI via rotation-invariant concise dictionaries, flexible K-space undersampling, and multiscale spatial regularity. In *IEEE International Symposium on Biomedical Imaging*, pages 9–12, 2013.
- [5] P.J. Basser, J. Mattiello, and D. LeBihan. Estimation of the effective self-diffusion tensor from the NMR spin echo. *Journal of Magnetic Resonance*, 103(3):247–254, 1994.
- 360 [6] A. Beck and M. Teboulle. A fast iterative shrinkage-thresholding algorithm for linear inverse problems. *SIAM Journal on Imaging Sciences*, 2(1):183–202, 2009.
- [7] B. Bilgic, K. Setsompop, J. Cohen-Adad, A. Yendiki, L. L Wald, and E. Adalsteinsson. Accelerated diffusion spectrum imaging with compressed sensing using adaptive dictionaries. *Magnetic Resonance in Medicine*, 68(6):1747–1754, 2012.
- [8] S. Boyd, N. Parikh, E. Chu, B. Peleato, and J. Eckstein. Distributed optimization and statistical learning via the alternating direction method of multipliers. *Foundations and Trends in Machine Learning*, 3(1):1–122, 2010.
- 365 [9] C. F. Caiafa and A. Cichocki. Computing sparse representations of multidimensional signals using kronecker bases. *Neural Computation*, 25(1):186–220, 2013.
- [10] Cesar F Caiafa and Franco Pestilli. Sparse multiway decomposition for analysis and modeling of diffusion imaging and tractography. *arXiv preprint arXiv:1505.07170*, 2015.
- 370 [11] E. Candès, L. Demanet, D. Donoho, and L. Ying. Fast discrete curvelet transforms. *Multiscale Modeling & Simulation*, 5(3):861–899, 2006.
- [12] Tzu-Cheng Chao, Jr-yuan George Chiou, Stephan E. Maier, and Bruno Madore. Fast diffusion imaging with high angular resolution. *Magnetic Resonance in Medicine*, 7:696–706, 2017.
- [13] J. Cheng, D. Shen, P. J. Basser, and P. T. Yap. Joint 6D kq space compressed sensing for accelerated high angular resolution diffusion MRI. In *Information Processing in Medical Imaging*, pages 782–793. Springer, 2015.

375 [14] Jian Cheng, Tianzi Jiang, Rachid Deriche, Dinggang Shen, and Pew-Thian Yap. Regularized spherical polar fourier diffusion MRI with optimal dictionary learning. In *International Conference on Medical Image Computing and Computer-Assisted Intervention*, pages 639–646. Springer, 2013.

380 [15] Jian Cheng, Sylvain Merlet, Emmanuel Caruyer, Aurobrata Ghosh, Tianzi Jiang, and Rachid Deriche. Compressive sensing ensemble average propagator estimation via l1 spherical polar fourier imaging. In *MICCAI Workshop on Computational Diffusion MRI*, 2011.

[16] Jian Cheng, Dinggang Shen, Pew-Thian Yap, and Peter J Basser. Tensorial spherical polar fourier diffusion mri with optimal dictionary learning. In *International Conference on Medical Image Computing and Computer-Assisted Intervention*, pages 174–182. Springer, 2015.

385 [17] Alessandro Daducci, Erick J Canales-Rodríguez, Hui Zhang, Tim B Dyrby, Daniel C Alexander, and Jean-Philippe Thiran. Accelerated microstructure imaging via convex optimization (AMICO) from diffusion MRI data. *NeuroImage*, 105:32–44, 2015.

[18] D. L. Donoho, M. Elad, and V. N. Temlyakov. Stable recovery of sparse overcomplete representations in the presence of noise. *IEEE Trans. on Information Theory*, 52(1):6–18, Jan. 2006.

390 [19] M. F. Duarte and R. G. Baraniuk. Kronecker compressive sensing. *IEEE Transactions on Image Processing*, 21(2):494–504, 2012.

[20] Julio M Duarte-Carvajalino, Christophe Lenglet, Kamil Ugurbil, Steen Moeller, Lawrence Carin, and Guillermo Sapiro. A framework for multi-task Bayesian compressive sensing of DW-MRI. In *MICCAI Workshop on Computational Diffusion MRI*, pages 1–13, 2012.

395 [21] Julio M Duarte-Carvajalino, Christophe Lenglet, Junqian Xu, Essa Yacoub, Kamil Ugurbil, Steen Moeller, Lawrence Carin, and Guillermo Sapiro. Estimation of the CSA-ODF using Bayesian compressed sensing of multi-shell HARDI. *Magnetic Resonance in Medicine*, 72(5):1471–1485, 2014.

[22] A. Goh, C. Lenglet, P.M. Thompson, and R. Vidal. Estimating orientation distribution functions with probability density constraints and spatial regularity. In *Medical Image Computing and Computer Assisted Intervention*, volume 5761, pages 877–885, 2009.

400 [23] H. R. Goncalves. *Accelerated Sparse Coding with Overcomplete Dictionaries for Image Processing Applications*. PhD thesis, 2015.

[24] A. Gramfort, C. Poupon, and M. Descoteaux. Sparse DSI: Learning DSI structure for denoising and fast imaging. In *Medical Image Computing and Computer Assisted Intervention*, pages 288–296. Springer, 2012.

405 [25] A. Gramfort, C. Poupon, and M. Descoteaux. Denoising and fast diffusion imaging with physically constrained sparse dictionary learning. *Medical Image Analysis*, 18(1):36–49, 2014.

[26] Simon Hawe, Matthias Seibert, and Martin Kleinsteuber. Separable dictionary learning. In *IEEE Conference on Computer Vision and Pattern Recognition*, pages 438–445, 2013.

410 [27] Daniela Kuhnt, Miriam H. A. Bauer, Jens Sommer, Dorit Merhof, and Christopher Nimsky. Optic radiation fiber tractography in glioma patients based on high angular resolution diffusion imaging with compressed sensing compared with diffusion tensor imaging - initial experience. *PLoS ONE*, 8(7):1–7, 07 2013.

[28] Daniela Kuhnt, Miriam HA Bauer, Jan Egger, Mirco Richter, Tina Kapur, Jens Sommer, Dorit Merhof, and Christopher Nimsky. Fiber tractography based on diffusion tensor imaging compared with high-angular-resolution diffusion imaging with compressed sensing: initial experience. *Neurosurgery*, 72(0 1):165, 2013.

[29] Bennett A Landman, John A Bogovic, Hanlin Wan, Fatma El Zahraa ElShahaby, Pierre-Louis Bazin, and Jerry L Prince. Resolution of crossing fibers with constrained compressed sensing using diffusion tensor MRI. *NeuroImage*, 59(3):2175–2186, 2012.

[30] M. Lustig, D. Donoho, and J.M. Pauly. Sparse MRI: The application of compressed sensing for rapid MR imaging. *Magnetic Resonance in Medicine*, 58(6):1182–1195, 2007.

[31] M. Mani, M. Jacob, A. Guidon, V. Magnotta, and J. Zhong. Acceleration of high angular and spatial resolution diffusion imaging using compressed sensing with multichannel spiral data. *Magnetic Resonance in Medicine*, 73(1):126–138, 2015.

[32] Darryl McClymont, Irvin Teh, Hannah J Whittington, Vicente Grau, and Jürgen E Schneider. Prospective acceleration of diffusion tensor imaging with compressed sensing using adaptive dictionaries. *Magnetic Resonance in Medicine*, 2015.

[33] M.I. Menzel, E.T. Tan, K. Khare, J.I. Sperl, K.F. King, X. Tao, C.J. Hardy, and L. Marinelli. Accelerated diffusion spectrum imaging in the human brain using compressed sensing. *Magnetic Resonance in Medicine*, 66(5):1226–1233, 2011.

[34] S. Merlet, E. Caruyer, and R. Deriche. Parametric dictionary learning for modeling EAP and ODF in diffusion MRI. In *Medical Image Computing and Computer Assisted Intervention*, pages 10–17. Springer, 2012.

[35] S. Merlet, E. Caruyer, A. Ghosh, and R. Deriche. A computational diffusion MRI and parametric dictionary learning framework for modeling the diffusion signal and its features. *Medical Image Analysis*, 17(7):830–843, 2013.

[36] S. Merlet, J. Cheng, A. Ghosh, and R. Deriche. Spherical polar Fourier EAP and ODF reconstruction via compressed sensing in diffusion MRI. In *IEEE International Symposium on Biomedical Imaging*, pages 365–371. IEEE, 2011.

[37] S. Merlet and R. Deriche. Continuous diffusion signal, EAP and ODF estimation via compressive sensing in diffusion MRI. *Medical Image Analysis*, 17(5):556–572, 2013.

[38] Sylvain Merlet and Rachid Deriche. Compressed sensing for accelerated EAP recovery in diffusion MRI. In *MICCAI*, pages Page–14, 2010.

[39] O. Michailovich and Y. Rathi. On approximation of orientation distributions by means of spherical ridgelets. In *IEEE International Symposium on Biomedical Imaging*, pages 939–942. IEEE, 2008.

[40] O. Michailovich and Y. Rathi. Fast and accurate reconstruction of HARDI data using compressed sensing. In *Medical Image Computing and Computer Assisted Intervention*, pages 607–614. Springer, 2010.

[41] O. Michailovich and Y. Rathi. On approximation of orientation distributions by means of spherical ridgelets. *IEEE Transactions on Image Processing*, 19(2):461–477, 2010.

[42] O. Michailovich, Y. Rathi, and S. Dolui. Spatially regularized compressed sensing for high angular resolution diffusion imaging. *IEEE Transactions on Medical Imaging*, 30(5):1100–1115, 2011.

[43] L. Ning and et al. Sparse reconstruction challenge for diffusion MRI: Validation on a physical phantom to determine which acquisition scheme and analysis method to use? *Medical Image Analysis*, 26(1):316–331, 2015.

[44] L. Ning, K. Setsompop, O. V. Michailovich, N. Makris, M. E. Shenton, C.-F. Westin, and Y. Rathi. A joint compressed-sensing and super-resolution approach for very high-resolution diffusion imaging. *NeuroImage*, 125:386–400, 2016.

[45] Y. Ouyang, Y. Chen, and Y. Wu. Vectorial total variation regularisation of orientation distribution functions in diffusion weighted MRI. *International Journal of Bioinformatics Research and Applications*, 10(1):110–127, 2014.

[46] Y. Ouyang, Y. Chen, Y. Wu, and H. M. Zhou. Total variation and wavelet regularization of orientation distribution functions in diffusion MRI. *Inverse Problems and Imaging*, 7(2):565–583, 2013.

[47] Michael Paquette, Sylvain Merlet, Guillaume Gilbert, Rachid Deriche, and Maxime Descoteaux. Comparison of sampling strategies and sparsifying transforms to improve compressed sensing diffusion spectrum imaging. *Magnetic Resonance in Medicine*, 73(1):401–416, 2015.

[48] Na Qi, Yunhui Shi, Xiaoyan Sun, and Baocai Yin. TenSR: Multi-dimensional tensor sparse representation. In *IEEE Conference on Computer Vision and Pattern Recognition*, pages 5916–5925, June 2016.

[49] Y. Rathi, O. Michailovich, F. Laun, K. Setsompop, P. E. Grant, and C.-F. Westin. Multi-shell diffusion signal recovery from sparse measurements. *Medical Image Analysis*, 18(7):1143–1156, 2014.

[50] Y. Rathi, O. Michailovich, K. Setsompop, S. Bouix, M.E. Shenton, and C.-F. Westin. Sparse multi-shell diffusion imaging. In *Medical Image Computing and Computer Assisted Intervention*, pages 58–65. Springer, 2011.

[51] Timothy G Reese, Thomas Benner, Ruopeng Wang, David A Feinberg, and Van J Wedeen. Halving imaging time of whole brain diffusion spectrum imaging and diffusion tractography using simultaneous image refocusing in EPI. *Journal of Magnetic Resonance Imaging*, 29(3):517–522, 2009.

[52] Y. Rivenson and Adrian S. Compressed imaging with a separable sensing operator. *IEEE Signal Processing Letters*, 16(6):449–452, 2009.

[53] E. Schwab, B. Afsari, and R. Vidal. Estimation of non-negative ODFs using eigenvalue distribution of spherical functions. In *Medical Image Computing and Computer Assisted Intervention*, volume 7511, pages 322–330, 2012.

[54] E. Schwab, R. Vidal, and N. Charon. Spatial-Angular Sparse Coding for HARDI. In *Medical Image Computing and Computer Assisted Intervention*, pages 475–483. Springer, 2016.

[55] Kawin Setsompop, Julien Cohen-Adad, BA Gagoski, T Raji, Anastasia Yendiki, Boris Keil, Van J Wedeen, and Lawrence L Wald. Improving diffusion MRI using simultaneous multi-slice echo planar imaging. *Neuroimage*, 63(1):569–580, 2012.

[56] X. Shi, X. Ma, W. Wu, F. Huang, C. Yuan, and H. Guo. Parallel imaging and compressed sensing combined framework for accelerating high-resolution diffusion tensor imaging using inter-image correlation. *Magnetic resonance in medicine*, 73(5):1775–1785, 2015.

[57] J. Sun, E. Sakhaei, A. Entezari, and B. C. Vemuri. Leveraging EAP-Sparsity for Compressed Sensing of MS-HARDI in (k,q)-Space. In *Information Processing in Medical Imaging*, pages 375–386. Springer, 2015.

[58] Jiaqi Sun, Yuchen Xie, Wenxing Ye, Jeffrey Ho, Alireza Entezari, Stephen J Blackband, and Baba C Vemuri. Dictionary learning on the manifold of square root densities and application to reconstruction of diffusion propagator fields. In *International Conference on Information Processing in Medical Imaging*, pages 619–631. Springer, 2013.

[59] A. Tristán-Vega and C.-F. Westin. Probabilistic ODF estimation from reduced HARDI data with sparse regularization. In *Medical Image Computing and Computer Assisted Intervention*, pages 182–190. Springer, 2011.

[60] J. Tropp. Greed is good: Algorithmic results for sparse approximation. *IEEE Transactions on Information Theory*, 50(10):2231–2242, Oct. 2004.

[61] D.S. Tuch. Q-ball imaging. *Magnetic Resonance in Medicine*, 52(6):1358–1372, 2004.

[62] V.J. Wedeen, P. Hagmann, W.Y. Tseng, T.G. Reese, and R.M. Weisskoff. Mapping complex tissue architecture with diffusion spectrum magnetic resonance imaging. *Magnetic Resonance in Medicine*, 54(6):1377–1386, 2005.

[63] S. Wolfers, E. Schwab, and R. Vidal. Nonnegative ODF estimation via optimal constraint selection. In *IEEE International Symposium on Biomedical Imaging*, pages 734–737, 2014.

[64] Yu-Chien Wu and Andrew L Alexander. Hybrid diffusion imaging. *NeuroImage*, 36(3):617–629, 2007.

[65] Chuyang Ye. Fiber orientation estimation using nonlocal and local information. In *Medical Image Computing and Computer Assisted Intervention*, pages 97–105. Springer, 2016.

[66] Chuyang Ye and Jerry L Prince. Probabilistic tractography using Lasso bootstrap. *Medical Image Analysis*, 35:544–553, 2017.

[67] W. Ye, B. C. Vemuri, and A. Entezari. An over-complete dictionary based regularized reconstruction of a field of ensemble average propagators. In *IEEE International Symposium on Biomedical Imaging*, pages 940–943. Springer, 2012.

[68] Shi Yin, Xinge You, Weiyong Xue, Bo Li, Yue Zhao, Xiao-Yuan Jing, Patrick SP Wang, and Yuanyan Tang. A Unified Approach for Spatial and Angular Super-Resolution of Diffusion Tensor MRI. In *Chinese Conference on Pattern Recognition*, pages 312–324. Springer, 2016.

[69] B. Yoldemir, M. Bajammal, and R. Abugharbieh. Dictionary Based Super-Resolution for Diffusion MRI. In *MICCAI Workshop on Computational Diffusion MRI*, pages 203–213. Springer, 2014.

[70] C. You, C.-G. Li, D. Robinson, and R. Vidal. Oracle based active set algorithm for scalable elastic net subspace clustering. In *IEEE Conference on Computer Vision and Pattern Recognition*, pages 3928–3937, 2016.